



OPEN

## Structural investigation of *Trypanosoma cruzi* Akt-like kinase as drug target against Chagas disease

Karina A. Stadler<sup>1,9</sup>, Lesly J. Ortiz-Joya<sup>1,2,7,9</sup>, Amit Singh Sahrawat<sup>3,4</sup>, Christoph Buhheller<sup>3</sup>, Karl Gruber<sup>3,4,5,6</sup>, Tea Pavkov-Keller<sup>3,5,6</sup>, Treasa B. O'Hagan<sup>7</sup>, Alba Guarné<sup>7</sup>, Sergio Pulido<sup>2,8</sup>, Marcel Marín-Villa<sup>2</sup>, Klaus Zangger<sup>1,5,6</sup>✉ & Nina Gubensäk<sup>3</sup>✉

According to the World Health Organization, Chagas disease (CD) is the most prevalent poverty-promoting neglected tropical disease. Alarming, climate change is accelerating the geographical spreading of CD causative parasite, *Trypanosoma cruzi*, which additionally increases infection rates. Still, CD treatment remains challenging due to a lack of safe and efficient drugs. In this work, we analyze the viability of *T. cruzi* Akt-like kinase (TcAkt) as drug target against CD including primary structural and functional information about a parasitic Akt protein. Nuclear Magnetic Resonance derived information in combination with Molecular Dynamics simulations offer detailed insights into structural properties of the pleckstrin homology (PH) domain of TcAkt and its binding to phosphatidylinositol phosphate ligands (PIP). Experimental data combined with Alpha Fold proposes a model for the mechanism of action of TcAkt involving a PIP-induced disruption of the intramolecular interface between the kinase and the PH domain resulting in an open conformation enabling TcAkt kinase activity. Further docking experiments reveal that TcAkt is recognized by human inhibitors PIT-1 and capivasertib, and TcAkt inhibition by UBMC-4 and UBMC-6 is achieved via binding to TcAkt kinase domain. Our in-depth structural analysis of TcAkt reveals potential sites for drug development against CD, located at activity essential regions.

**Keywords** American trypanosomiasis, Parasitic disease, NMR, Akt/PKB, PH domain

CD is a potentially chronic and life-threatening disease caused by the protozoan parasite *Trypanosoma cruzi*, which is classified by the World Health Organization (WHO) as the most prevalent of poverty promoting neglected tropical diseases<sup>1</sup>. CD is endemic in Latin America and is gradually turning into a global health problem due to globalization and climate change<sup>2–6</sup>.

Parasite transmission from *T. cruzi* to the human host is primarily vector-borne via direct interaction with infected Triatominae bugs. Other transmission routes include oral ingestion of contaminated products, transplacental passage from mother to fetus, blood transfusions and organ transplantations from infected donors<sup>7,8</sup>. The clinical spectrum of CD is broad and potentially causes fatal chronic illness like cardiomyopathy, gastrointestinal or neurological diseases<sup>1,7,8</sup>.

The current treatment relies on two drugs developed more than five decades ago: nifurtimox and benznidazole<sup>2,9</sup>. These nitroheterocyclic drugs require long treatment periods, are ineffective in chronic stages of CD and are associated with a high prevalence of toxic side-effects leading to discontinued treatments<sup>10</sup>. Emerging resistant *T. cruzi* strains against both drugs also raise the demand for new molecular targets and treatment options against CD<sup>11</sup>.

<sup>1</sup>Institute of Chemistry/Organic and Bioorganic Chemistry, University of Graz, Graz, Austria. <sup>2</sup>Programa de Estudio y Control de Enfermedades Tropicales (PECET), Facultad de Medicina, Universidad de Antioquia, Medellín, Colombia. <sup>3</sup>Institute of Molecular Biosciences, University of Graz, Graz, Austria. <sup>4</sup>Innophore GmbH, Graz, Austria. <sup>5</sup>Field of Excellence BioHealth, University of Graz, Graz, Austria. <sup>6</sup>BioTechMed-Graz, Graz, Austria. <sup>7</sup>Department of Biochemistry, McGill University, Montreal, Canada. <sup>8</sup>LifeFactors ZF SAS, Rionegro, Colombia. <sup>9</sup>These authors contributed equally: Karina A. Stadler and Lesly J. Ortiz-Joya. ✉email: klaus.zangger@uni-graz.at; nina.gubensaek@uni-graz.at

Over the past few decades, many *T. cruzi* targets have been analyzed for drug development purposes<sup>12–21</sup>. However, until now none of those targets have led to new candidates in clinical trials yet<sup>9,22</sup>. In fact, the drug development pipeline for CD remains limited, even compared to other neglected diseases, like leishmaniasis<sup>22</sup>.

*TcAkt* was previously proposed as a promising target for the development of drugs against CD<sup>23,24</sup>. Akt kinases play a central role in all organisms as they are key regulators involved in the balance between growth, proliferation and apoptosis<sup>25,26</sup>. *TcAkt* inhibition causes apoptosis-like events in *T. cruzi*, confirming its essential role for the survival of the parasite<sup>23,24,27</sup>. Furthermore, *TcAkt* is present in all stages of the parasite life cycle—epimastigotes, trypomastigotes and amastigotes—which is crucial for effective treatment of CD. Considerable effort has been made to inhibit *TcAkt* based on bioinformatics and molecular docking studies<sup>23,24</sup>. However, the three-dimensional structure of the Akt-like kinase in trypanosomatids has not been determined yet, resulting in a lack of detailed information and understanding of its mechanism of action<sup>27</sup>.

Akt kinases, also called protein kinase B (PKB), contain an N-terminal pleckstrin homology (PH) domain, a catalytic (kinase) domain and a disordered, regulatory, C-terminal tail (C-tail)<sup>28</sup>. Regulation of human Akt (*HsAkt*), comprising of the isoforms Akt1, Akt2 and Akt3, involves the interaction of the PH and the kinase domain through the so-called ‘autoinhibitory intramolecular interface’<sup>25,26,28–30</sup>. In this autoinhibitory state, the PH domain is packed against the kinase domain, resulting in a closed conformation of *HsAkt*. In its autoinhibitory state, *HsAkt* is constitutively phosphorylated at T450 and primed with adenosine triphosphate (ATP) bound in a deep cleft between the N-terminal (N-lobe) and C-terminal lobe (C-lobe) of the kinase domain<sup>26,30</sup>. Upon recruitment of *HsAkt* to the plasma membrane, the PH domain binds to membrane-associated phosphatidylinositol-3,4,5-trisphosphate (PIP<sub>3</sub>) or phosphatidylinositol-3,4-bisphosphate (PI(3,4)P<sub>2</sub>), thereby inducing a disruption of the intramolecular interface<sup>26,31</sup> and forming an open conformation of *HsAkt*<sup>30</sup>. Dislodgement of the PH domain from the kinase domain, triggered by conformational changes in loop regions of the PH domain<sup>28,32</sup>, leads to subsequent phosphorylation of S473 and T308 and induces a re-orientation of the activation loop enabling high-affinity substrate binding and, in turn, full activation of *HsAkt*<sup>26,30</sup>.

The active site of Akt kinases contains several structural elements that are necessary for substrate phosphorylation: the glycine-rich G-loop involved in ATP-binding, the activation loop binding the peptide substrate and the catalytic loop<sup>33,34</sup>. Precise interactions between these elements create an environment for phosphotransfer to substrates that contain the characteristic motif RXXRX(S/T)f, with f representing a large hydrophobic residue<sup>35–41</sup>. Phosphorylation of these targets on serine or threonine residues leads to activation or inhibition of the given protein<sup>35,36</sup>.

A crucial step in the activation represents the binding of the PH domain to membrane-associated PIPs to induce specific cellular processes<sup>42–46</sup>. *T. cruzi* expresses all necessary enzymes to synthesize PI(3,4,5)P<sub>3</sub> as well as PI(3,4)P<sub>2</sub>, PI(3,5)P<sub>2</sub> and PI(4,5)P<sub>2</sub><sup>44,47,48</sup>. Each of those PIP residues is associated with distinctive molecular functions: PI(3,4,5)P<sub>3</sub> is involved in actin polymerization, cell survival and cell growth, PI(3,5)P<sub>2</sub> plays a crucial role in homeostasis and stimuli response, whereas PI(4,5)P<sub>2</sub> is important for cell migration, gene expression and endo-/exocytosis<sup>44</sup>. Still, the understanding of the signaling mechanisms of PIPs and involved enzymes remains elusive and needs to be investigated further<sup>44,47–49</sup>.

Two putative phosphorylation sites (p-sites) could be identified in *T. cruzi* by multiple sequence alignment (MSA), T290 in the activation loop and S450 in the hydrophobic motif (h-motif)<sup>27</sup>. While these sites have not been experimentally confirmed in *T. cruzi*, the phosphorylation of an equivalent threonine in *Leishmania panamensis*—a closely related trypanosomatid parasite—could be experimentally detected<sup>50</sup>.

The phosphorylation motif RXXRX(S/T)f is a common consensus sequence recognized by protein kinases and was detected with a 1.74% abundance in the *T. cruzi* phosphoproteome at the epimastigotes, a replicative form of the parasite that colonize the digestive tract of the vector<sup>37</sup>. A short version of this motif, the RXXS sequence, represents a phosphorylation motif during the differentiation process from trypomastigotes to amastigotes. It could be identified in phosphoproteins associated with processes that are highly relevant to the differentiation stimulus–response such as cell communication, cellular organization, and biogenesis<sup>51</sup>. Analysis of the *T. cruzi* genome exhibits several homologs to identified human Akt substrates<sup>38–40</sup>, thus presenting putative *TcAkt* targets: glycogen synthase kinase 3 GSK-3 (TritypDB ID: TcCLB.507993.80), ribosomal protein S6 (ID: TcCLB.508277.120), Rab11 (ID: TcCLB.511407.60) and glyceraldehyde-3-phosphate dehydrogenase TcGAPDH (ID: TcCLB.506885.413)<sup>41</sup>. However, further in vitro and in vivo experiments are needed to identify and confirm putative *TcAkt* substrates.

In this work, we present the first experimentally determined structure of an Akt-like protein domain of a protozoan parasite. Our NMR solution structure of *TcAkt*-PH reveals a typical PH domain fold including a basic charged cleft. By using NMR Chemical Shift Perturbation (CSP) experiments<sup>52,53</sup> we confirm the binding of inositol-1,3,4,5-tetraphosphate (Ins(1,3,4,5)P<sub>4</sub>), the soluble headgroup of PIP<sub>3</sub>, to *TcAkt*-PH inducing local conformational changes of loop regions  $\beta$ 1– $\beta$ 2,  $\beta$ 3– $\beta$ 4 and  $\beta$ 6– $\beta$ 7, affecting its dynamics. The presented experiments reveal that phosphorylation patterns of inositol headgroups induce distinctive conformational changes either stabilizing or destabilizing loop-to-helix transitions suggesting that dynamics of loop regions of *TcAkt*-PH play a crucial role in regulating versatile Akt-like functionality. By combining experimental information with Alpha Fold (AF) calculations we present a model for the mechanism of action of *TcAkt* involving a PIP-induced disruption of the autoinhibitory intramolecular interface between the *TcAkt* kinase and PH domain, via bending of *TcAkt*-PH loop  $\beta$ 1– $\beta$ 2 upon ligand interaction. The molecular docking derived structure of ATP-bound *TcAkt* reveals strong similarities to *HsAkt* unravelling activity essential residues. Further docking experiments show that human Akt inhibitors PIT-1<sup>32,54</sup> and capivasertib<sup>55,56</sup> recognize *TcAkt* via similar binding modes compared to *HsAkt*. Additionally, based on the AF structure of *TcAkt*, the exact localization of the binding site of previously described *TcAkt* inhibitors UBMC-4<sup>23</sup> and UBMC-6<sup>24</sup> could be determined at the kinase domain of *TcAkt*, thus suggesting kinase-involved inhibition modes.

The presented experiments offer primary insights into the structure and function of the central protein Akt-like of a protozoan parasite and furthermore reveal potential drug target regions crucial for *TcAkt* function but exhibiting significant structural differences to *HsAkt*. The detailed understanding of the mechanism of action of *TcAkt* forms the basis for the development of effective drugs against the expanding CD.

## Results

### N-terminal *TcAkt*-PH forms a positively charged flexible cleft

The presented NMR solution structure of the membrane binding domain *TcAkt* represents to date the only experimentally determined structure of an Akt-like protein domain of a protozoan parasite. The structural determination of *TcAkt*-PH (11.7 kDa, 100 aa) was achieved by a combination of NMR experimental data including long range NOEs and CS-Rosetta<sup>57</sup> (Figs. 1a, S1a, Tables S1, S2, and S3). The following structural analysis is based on the lowest energy structure of *TcAkt*-PH (PDB: 8OZZ) (Fig. 1b).

*TcAkt*-PH has a typical PH domain fold<sup>46,59</sup> consisting of a C-terminal  $\alpha$ -helix and two antiparallel  $\beta$ -sheets, formed by four and three  $\beta$ -strands, respectively (Fig. 1b,c). All structural elements (strands  $\beta$ 1– $\beta$ 7, helix  $\alpha$ 1) contribute to the formation of the hydrophobic core (Fig. S1) resulting in a stable structure with an averaged rotational correlation time of 8.68 ns (Eq. 2), as observed by NMR relaxation experiments (Fig. S2a–d). Additionally, *TcAkt*-PH exposes an intense network of seven surface-exposed intramolecular salt bridges, providing further stabilization of the fold (Fig. S3). Expression constructs of C-terminal truncated *TcAkt*-PH (aa 1–95), results in a destabilization of the structure, probably due to missing helix-stabilizing residues S96 and K97.

Calculation of the electrostatic surface potential (see Eq. 1) in combination with NMR relaxation analysis (Figs. 2b and S2a) reveals a dynamic, positively charged cleft of *TcAkt*-PH (Fig. 2a) gated by three flanking loops  $\beta$ 1– $\beta$ 2,  $\beta$ 3– $\beta$ 4 and  $\beta$ 6– $\beta$ 7, which include nine basic charged residues (K11, R23, K15, K18, K19, K36, R37, R38, K76) (zoomed details in Fig. 2a).

### Phosphoinositides bind into the basic cleft of *TcAkt*-PH

To analyze if *TcAkt*-PH binds to PIP ligands, we performed NMR CSP experiments using the soluble headgroup  $\text{Ins}(1,3,4,5)\text{P}_4$  of the proposed ligand  $\text{PI}(3,4,5)\text{P}_3$  (Figs. S4 and S5). The experiments confirmed an interaction of  $\text{Ins}(1,3,4,5)\text{P}_4$  with *TcAkt*-PH exhibiting a dissociation constant of  $40 \pm 14 \mu\text{M}$  (Table S4). NMR  $^1\text{H}$ - $^{15}\text{N}$  HSQC spectra of *TcAkt*-PH were recorded before and after the addition of increasing amounts of the ligand (Fig. S5). NMR chemical shifts are sensitive to their local chemical environment. Thereby, residues involved in direct interaction with a ligand can be detected via the degree of change of their chemical shift compared to the apo-form<sup>52</sup>. Residues directly located in the binding pocket generally exhibit a strong change of their chemical shift and/or peak intensity. Residues that do not bind to the ligand directly but experience ligand-induced conformational changes, can also be detected via CSP. For each amino acid of *TcAkt*-PH, the Euclidean distance or  $d$ -value was calculated (Eq. 4) (Fig. 3a,b), defined as combined value of  $^{15}\text{N}$ - and  $^1\text{H}$ -shifts, thus representing the degree of change of the chemical shift of a specific residue upon ligand addition and its involvement in the ligand interaction (Fig. 3a,b).

The presented experimental data reveals that ligand-induced conformational changes affect mainly residues in or at close proximity to the positively charged cavity of *TcAkt*-PH including loops  $\beta$ 1– $\beta$ 2,  $\beta$ 3– $\beta$ 4, and  $\beta$ 6– $\beta$ 7, thus facilitating the required opposite charge for interactions with phosphate groups of  $\text{Ins}(1,3,4,5)\text{P}_4$  (Figs. 2a and 3a,b). In detail, high  $d$ -values could be determined for strands  $\beta$ 1,  $\beta$ 2 and connecting  $\beta$ 1– $\beta$ 2 loop involving residues: T12, G13, G14, F16, Y17, N20, Q21 and T22 (Fig. 3a). Significant chemical shift changes could be furthermore detected for residues located at strands  $\beta$ 3,  $\beta$ 4 and loop  $\beta$ 3– $\beta$ 4 (Y34, R38, T47) as well as strands  $\beta$ 6,  $\beta$ 7 and loop  $\beta$ 6– $\beta$ 7 (S66–T81). Residues of loop  $\beta$ 4– $\beta$ 5 (A55, R56) are probably affected indirectly by the ligand interaction due to conformational changes since their location is spatially distant from the binding site. Chemical shift changes of basic residues K11, K15, K18, K19 and R23, located in strands  $\beta$ 1,  $\beta$ 2 and loop  $\beta$ 1– $\beta$ 2, could not be analyzed in the  $^1\text{H}$ - $^{15}\text{N}$  HSQC spectrum due to missing signals or spectral overlap. Nevertheless, surrounding residues are highly influenced by ligand binding (Fig. 3a), thus suggesting that the mentioned basic amino acids play a crucial role in the interaction with  $\text{Ins}(1,3,4,5)\text{P}_4$ .

Subsequent Molecular Dynamics (MD) simulations in combination with NMR experimental data reveal that the nature of the protein–ligand interactions between *TcAkt*-PH and  $\text{Ins}(1,3,4,5)\text{P}_4$  is strictly polar including H-bonds, ionic interactions and water bridges (Fig. 3d, see SI Section 1, Fig. S7). Except for R38 and K19, all basic charged residues located in the positively charged cleft are interacting with the ligand (Figs. 2a and S6). Additionally, N20 has profound interactions with  $\text{Ins}(1,3,4,5)\text{P}_4$ , as well as Y34 and T47, which form water-mediated interactions (Fig. 3c,d). Interestingly, N20 faces away from the binding site in the apo-form of *TcAkt* but when bound to  $\text{PIP}_3$ , N20 rotates towards the ligand, enabling interactions with PIP phosphate groups (Fig. 3b,c).

### *TcAkt* PH domain undergoes local conformational changes while hosting $\text{Ins}(1,3,4,5)\text{P}_4$

For analyzing the impact of ligand interaction on *TcAkt*-PH dynamics,  $\{^1\text{H}\}$ - $^{15}\text{N}$  heteronuclear NOE (hetNOE) experiments were recorded before and after  $\text{Ins}(1,3,4,5)\text{P}_4$  addition (Fig. 4a). As shown in Fig. 4b, ligand binding induces a slight increase of rigidity of residues located at the binding site (loop regions  $\beta$ 1– $\beta$ 2 and  $\beta$ 6– $\beta$ 7) or close to the binding cleft of *TcAkt*-PH (strand  $\beta$ 3 and loop  $\beta$ 3– $\beta$ 4), whereas the dynamics of the rest of the protein are not affected (Fig. 4b,c).

As shown by MD simulations the increase of rigidity observed by NMR can be explained by ligand-induced loop-to-helix transitions. The apo-form of *TcAkt*-PH already reveals a tendency for loop-to-helix transitions (Figs. 5a, S8a, and S9). However, binding of  $\text{Ins}(1,3,4,5)\text{P}_4$  further stabilizes mentioned conformational changes for a more extended period (Figs. 5a, S8b, and S9).

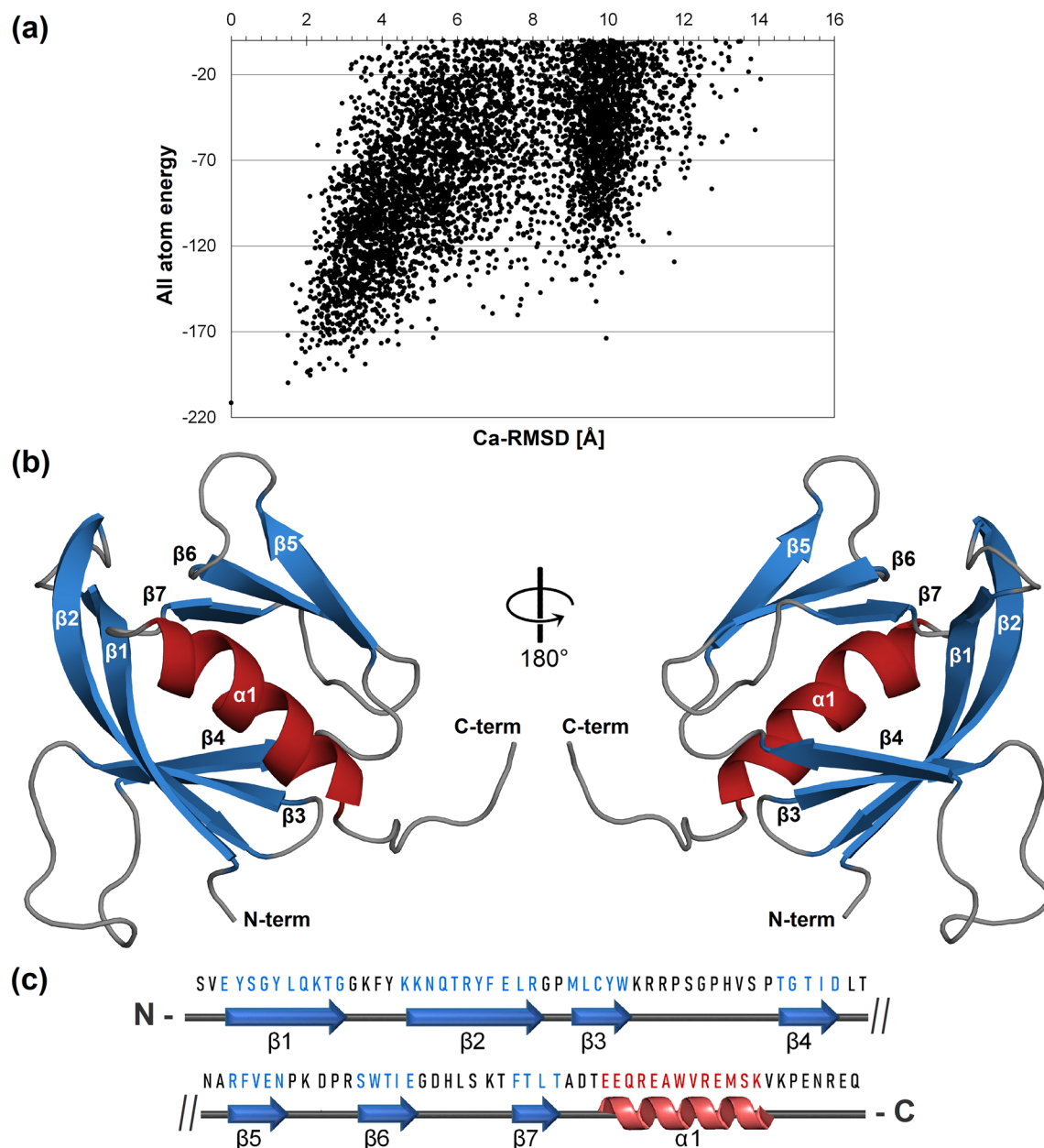


**Figure 1.** NMR derived structure of *TcAkt-PH* (PDB: 8OZZ) (a) CS-Rosetta<sup>57,58</sup> plot: All atom energies of *TcAkt-PH* models with respect to their Ca-RMSD values relative to the lowest-energy model. 10 000 structures were calculated. For each structure the Ca-RMSD to the lowest-energy structure (S\_07667) was calculated and plotted against the all-atom energy of each model. The run is designated as converged due to the shape of the plot and the averaged Ca-RMSD value of 1.7 Å of the final 10 structures to the lowest-energy model (S\_07667). (b) Lowest energy structure as cartoon representation: *TcAkt-PH* forms a typical PH domain fold, built of two antiparallel β-sheets shown in blue (β1-β4, β5-β7) and a C-terminal α-helix α1 (red). Loops are shown in grey. (c) Topology and amino acid sequence of *TcAkt-PH* (aa 2–105).

Although regions 41–43 (SGP) and 46–48 (PTG) are both located in loop β3-β4, Ins(1,3,4,5)P<sub>4</sub> interaction seems to have different effects on the dynamics and conformations of the stretches. Stretch 41–34 is more solvent exposed and experiences an increase of flexibility upon ligand interaction (Figs. 4c and S9) whereas stretch 46–48 is closer to strand β4 and its helical tendency is stabilized when Ins(1,3,4,5)P<sub>4</sub> is bound (Fig. S9).

Eventually, Ins(1,3,4,5)P<sub>4</sub> pulls the loops β3-β4 and β6-β7 towards the binding site compared to their respective conformations in the apo-form (Fig. 4c). Consequently, loop β1-β2 changes into a more open conformation upon Ins(1,3,4,5)P<sub>4</sub> binding, compared to the compact, apo-form (Fig. 4c).

### Phosphorylation patterns of PIP ligands induce different conformational changes of *TcAkt-PH*

As previously stated, PIPs act as signaling molecules involved in numerous cellular pathways depending on the position of phosphate groups on their inositol ring guiding broad Akt functionality<sup>42–44</sup>.

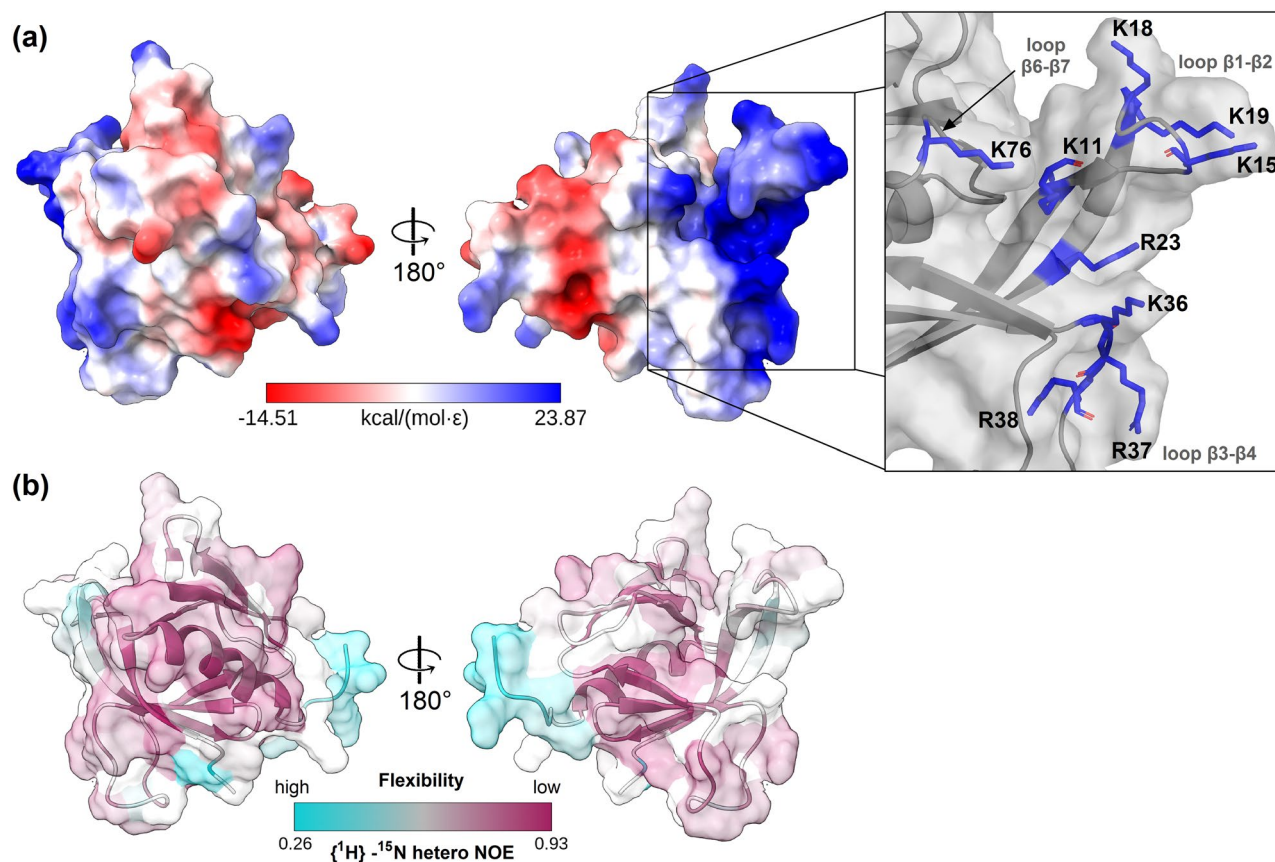


**Figure 2.** Surface representation of electrostatic potential and flexibility of *TcAkt*-PH. **(a)** Electrostatic surface of *TcAkt*-PH apo-form (PDB: 8OZZ) with zoomed details of nine basic amino acids: K11 ( $\beta$ 1); R23 ( $\beta$ 2); K15, K18, K19 (loop  $\beta$ 1- $\beta$ 2); K36, R37, R38 (loop  $\beta$ 3- $\beta$ 4); K76 (loop  $\beta$ 6- $\beta$ 7). Coulombic electrostatic potential (kcal/(mol $\cdot$  $\epsilon$ )) at 298 K was calculated using ChimeraX<sup>60-62</sup> (see Eq. 1). Negative electrostatic potential is shown in red (min: -14.51), positive electrostatic potential in blue (max: 23.87). **(b)** Transparent surface with display of hetNOE values (see Eq. 3) of *TcAkt*-PH apo-form: low hetNOE values are colored in cyan, high hetNOE values in purple, not assigned (n.a.) residues in white. Orientation is consistent with Fig. 1b.

To monitor the binding behavior of different PIP ligands to *TcAkt*-PH, MD simulations were performed using inositol phosphates (InsP): Ins(1,3,4,5)P<sub>4</sub>, Ins(1,3,4)P<sub>3</sub>, Ins(1,3,5)P<sub>3</sub> and Ins(1,4,5)P<sub>3</sub> (Fig. S4). According to MD data, all InsP ligands bind in the same cavity of *TcAkt*-PH and remain bound throughout the 2  $\mu$ s MD run (Figs. 3c and 5b-d), exhibiting RMSD values less than 1.5 Å (Fig. S10b) which indicates a stable interaction<sup>63</sup>. Ins(1,3,4,5)P<sub>4</sub> shows the strongest binding due to an additional phosphate group. Similar interaction energies IE (Fig. S10a) could be calculated for other InsP ligands.

Although tested ligands bind into the same cavity of *TcAkt*-PH, ligand-induced conformational changes of *TcAkt*-PH loop regions are versatile and complex as shown in detail in Fig. 5a (Figs. S8 and S9). Phosphorylation patterns of PIP headgroups impact distinctive conformational changes of *TcAkt* loops  $\beta$ 1- $\beta$ 2,  $\beta$ 3- $\beta$ 4 and  $\beta$ 4- $\beta$ 5, resulting in ligand-specific structural rearrangements of the PH domain, which subsequently could influence the versatile functionalities of *TcAkt*<sup>43,44</sup>. Still, all of the tested ligands induce a similar bending of loop  $\beta$ 1- $\beta$ 2 when binding to *TcAkt*-PH, independent on their phosphorylation pattern (Fig. S11).

### *TcAkt*-PH prefers PIP ligands with P3 and P5 phosphorylations

In humans, a binding preference of Akt1 PH domain to PI(3,4,5)P<sub>3</sub> and PI(3,4)P<sub>2</sub><sup>26,32,42,64</sup> was determined by monitoring its intrinsic tryptophane fluorescence upon binding to different inositol phosphates<sup>65</sup>, as well as by competitive HPLC binding experiments of <sup>32</sup>P-labeled phosphoinositides<sup>66</sup>. To analyze *TcAkt* binding preferences, we calculated the solvent-accessible surface area (SASA) and the buried surface area (BSA) of each of the tested ligands when bound to *TcAkt*-PH (Fig. S10d). The more buried a ligand is in the binding site, the larger its BSA will be. The extent of BSA increase is an important descriptor of ligand binding<sup>67,68</sup> and can therefore be used for analyzing the impact of different phosphorylation patterns of PIP ligands on the interaction with *TcAkt*-PH.

The calculated averaged BSA (Fig. S10d) shows no significant differences between all InsPs, reflecting that the depth of the binding pocket remains consistent and is equally accessible to all InsPs irrespective of the number and relative positions of phosphate groups on the inositol ring. However, when analyzing each phosphate position individually, different BSA values could be observed (Fig. S10c). Irrespective of the type of InsP, the P1 phosphate group has the lowest BSA, meaning that it is more exposed to the solvent relative to other phosphate positions. In

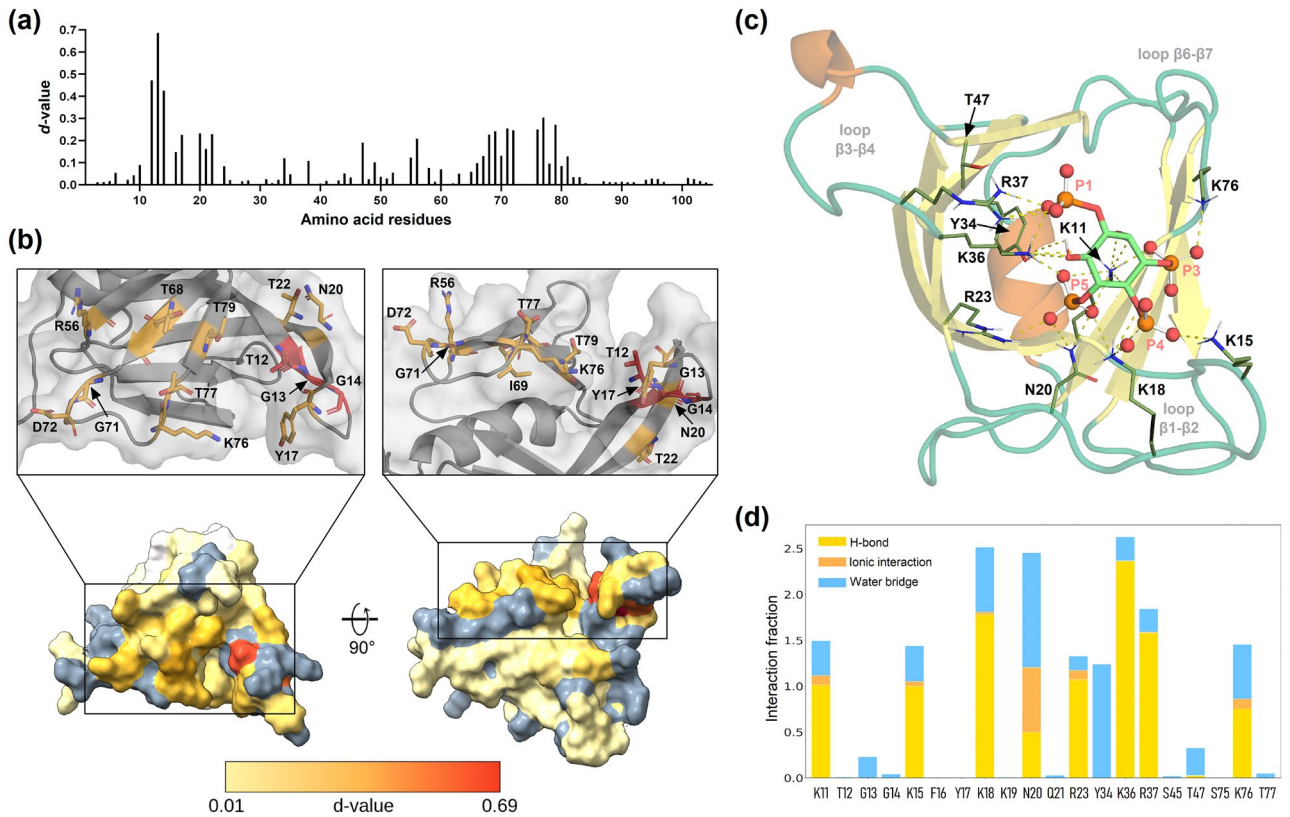


**Figure 3.** *TcAkt*-PH PIP binding site evaluation by NMR and MD simulations. **(a)** Chemical shift perturbations of *TcAkt*-PH. The graph includes calculated  $d$ -values (see Eq. 4) for each amino acid of *TcAkt*-PH. **(b)** Surface display of *TcAkt*-PH colored by determined  $d$ -values according to a gradient. Residues exhibiting high  $d$ -values are shown in red (max: 0.69), low  $d$ -values in light yellow (min: 0.01), not affected residues below threshold ( $<0.008$ ) in white, n.a. residues (due to overlap or missing peaks) are shown in grey. **(c)** MD derived structure of *TcAkt*-PH interacting with  $\text{Ins}(1,3,4,5)\text{P}_4$  (a frame was carefully chosen from the last 1  $\mu\text{s}$  MD simulation to showcase the interacting residues adequately): Interacting residues are shown in sticks, contacts in dashed yellow lines, phosphate groups in red (ball representation). **(d)** H-bonds, ionic interactions, and water bridges plotted as interaction fractions for each interacting residue: Bar charts are normalized over the course of the trajectory. A value of 1 indicates that the respective interaction type persists throughout 100% of the simulation time, while a value greater than 1 signifies multiple instances of the same interaction type between corresponding residue and ligand over the simulation duration (e.g., multiple hydrogen bonds between arginine and the ligand). Additional details on the computed interactions (H-bonds, ionic interactions, and water bridges) can be found in the supplementary information (SI Section 1 ‘Detailed description for computed protein–ligand interactions of *TcAkt*-PH and  $\text{Ins}(1,3,4,5)\text{P}_4$  shown in Fig. 3d’).

the membrane-bound PIP ligand, the fatty acid tail is attached on phosphate group P1 and is therefore oriented towards the membrane rather than the binding site and does not seem to form specific interactions with *TcAkt*.

In comparison, the P3 phosphorylation has the highest BSA values in all  $\text{InsPs}$ . For  $\text{Ins}(1,4,5)\text{P}_3$ , which lacks the P3 phosphate group, P5 seems to compensate for P3 with comparable BSA values. Thus, we propose a preference of *TcAkt*-PH for PIP ligands containing P3 and/or P5 phosphorylations.

As previously shown, MD data reveals that all PIP ligands induce a bending of loop  $\beta$ 1- $\beta$ 2 (Fig. S11). Nevertheless, different phosphorylation patterns of PIP ligands initiate different local conformational changes of *TcAkt* and also vary in binding behavior, thus supporting a ligand specificity of *TcAkt*. In contrast to *HsAkt1*, which favors P3 and P4 phosphorylations of PIP<sup>26,32,42,64</sup>, *TcAkt* shows a preference for P3 and P5 phosphate groups.

### The kinase domain of *TcAkt* contains conserved motifs essential for Akt activity

Since structure determination of full-length *TcAkt* by X-ray crystallography was not successful, we used AF<sup>69</sup> for calculating the structure of *TcAkt* (Figs. 6 and S12). According to internal quality parameters, the calculation runs were designated as successful (see Materials and Methods section ‘AF calculations’).

Crucial residues in regions associated with Akt activation are typically highly conserved among kinases and are also present in the AF *TcAkt* structure (Figs. 6 and S14): The glycine-rich G-loop in the kinase C-lobe is crucial for ATP binding and was stated to have the consensus sequence GXGX $\Phi$ G, with  $\Phi$  as hydrophobic residue<sup>33,34,56</sup>. While this is consistent with the G-loop in *HsAkt1*, in *TcAkt* the third glycine within this sequence is replaced by a serine (Fig. S14), an exception that is also found in other protein kinases<sup>70,71</sup>. The catalytic loop, also present in the C-lobe, is responsible for the phospho-transfer from ATP to the substrate and carries

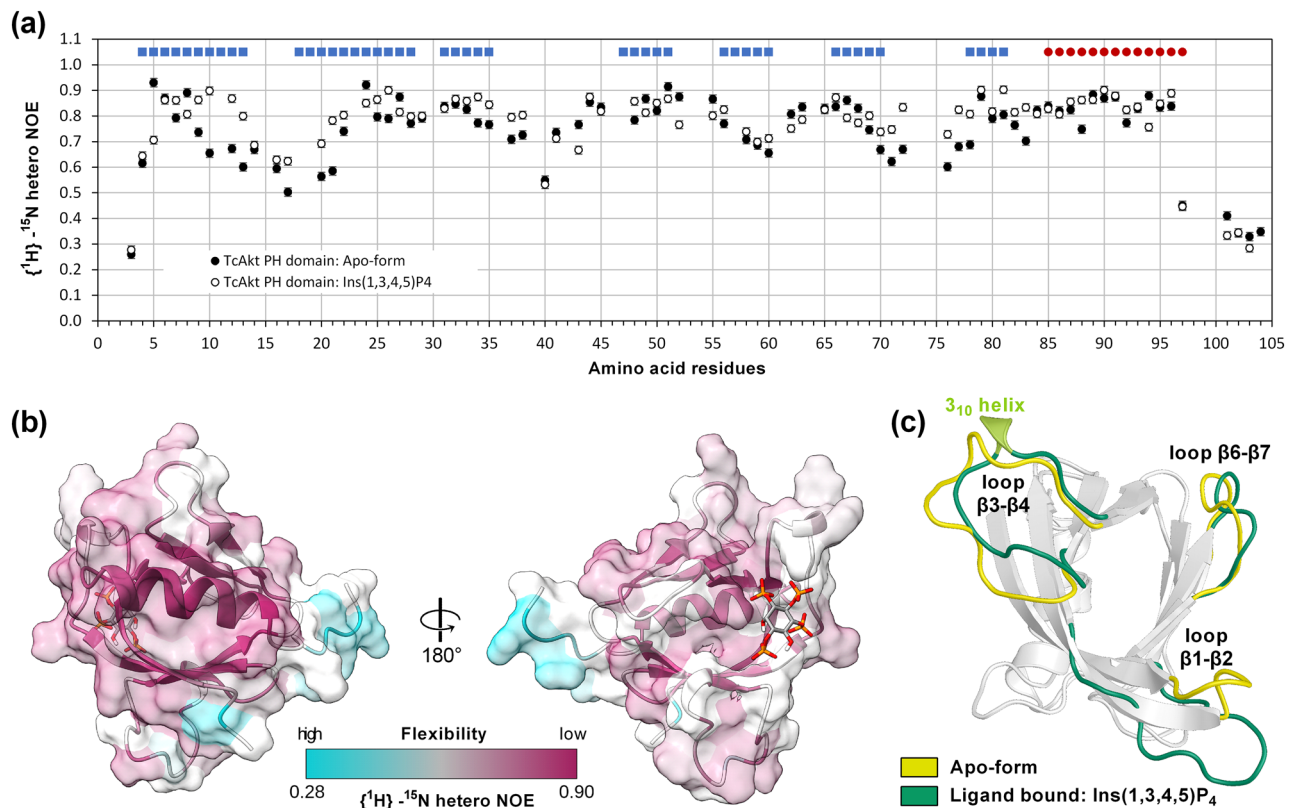


**Figure 4.** Conformational and dynamic changes of *TcAkt*-PH initiated by  $\text{Ins}(1,3,4,5)\text{P}_4$  binding. (a) Dynamic analysis of apo *TcAkt*-PH and  $\text{Ins}(1,3,4,5)\text{P}_4$  bound *TcAkt*-PH. The hetNOE values (see Eq. 3) of residues of apo *TcAkt*-PH are shown as black spheres. The hetNOE values of residues of *TcAkt*-PH bound to  $\text{Ins}(1,3,4,5)\text{P}_4$  are shown as white spheres. *TcAkt*-PH secondary structure elements are shown above the graph:  $\beta$ -strand forming residues are marked as blue squares, helix forming residues are represented as red spheres. (b) Structure of *TcAkt*-PH colored according to determined hetNOE values of *TcAkt*-PH bound to  $\text{Ins}(1,3,4,5)\text{P}_4$ : low hetNOE values are shown in cyan (min: 0.28), high hetNOE values in purple (max: 0.90), n.a. in white. Orientation of *TcAkt*-PH is consistent with Fig. 1b. (c) Structural superimposition of *TcAkt*-PH apo-form (yellow loops) and *TcAkt*-PH bound to  $\text{Ins}(1,3,4,5)\text{P}_4$  (green loops, light green  $3_{10}$  helix).

a conserved aspartic acid (in *TcAkt* D257) that interacts directly with the target S/T p-site (*Hs*: T308, *Tc*: T290) (Figs. S13 and S14)<sup>27,34,56</sup>. The activation loop starts with the highly conserved DFG motif and ends with the APE motif<sup>33,34</sup>, whereas the crucial threonine p-site (in *T. cruzi* T290) is located in between (Fig. S14). The h-motif is part of the C-tail and usually contains the sequence FXXF(S/T)(Y/F)<sup>27</sup> and a p-site. *TcAkt* shows a shortened version of the h-motif (FSF) including the putative p-site S450 (Figs. S13 and S14). Other p-sites in the C-tail that were linked to *HsAkt1* activation (*Hs*: S477, T479) are absent in *TcAkt*<sup>25,28,29</sup>.

### Full-length *TcAkt* retains kinase activity and possesses a similar ADP/ATP binding pocket compared to human Akt

To evaluate functional properties in a full-length context, we expressed and purified recombinant *TcAkt* (Fig. S15a) and tested its enzymatic activity in vitro using a polyclonal antibody that recognizes its phosphorylated form. The synthetic peptide RPRAATF was used as a substrate. As shown in Fig. S15b, *TcAkt* efficiently phosphorylates the threonine residue of the peptide substrate as did *HsAkt3*, which was used as a positive control. This indicates that *TcAkt* is capable of recognizing the consensus recognition motif RXXRX(S/T)f associated with Akt-mediated phosphorylation<sup>35–37</sup>.

Based on the presented AF structure, an ATP bound model of *TcAkt* was calculated using the recent release of RoseTTAFold All-Atom<sup>72</sup>. The protein–ligand model proposes that *TcAkt* binds ATP in a similar manner compared to *HsAkt2* in complex with AMP-PnP, an ATP analog, and  $\text{Mn}^{2+}$  (PDB: 1O6K) (Fig. 7), thus emphasizing a strong structural and sequential conservation in this region. Figure 7 shows the ATP binding site of *TcAkt* kinase domain with involvement of residues from the G-loop, the C-tail, the DFG motif, catalytic spine residues and shell residues<sup>56,75,76</sup>. According to Kornev et al.<sup>76</sup> catalytic spine residues of protein kinases, as well as the DFG motif, are essential for positioning ATP and  $\text{Mn}^{2+}$ , while shell residues were identified to have a stabilizing effect<sup>77</sup> (Fig. 7).

Differential scanning fluorimetry (DSF) experiments revealed an increased melting temperature ( $T_m$ ) upon ADP and ATP binding only in the presence of  $\text{Mn}^{2+}$  (Figs. S16 and S17). These findings match observations reported by Pascucci et al.<sup>71</sup>, showing that *TcAkt* requires  $\text{Mn}^{2+}$  to phosphorylate substrates in vitro, but is not

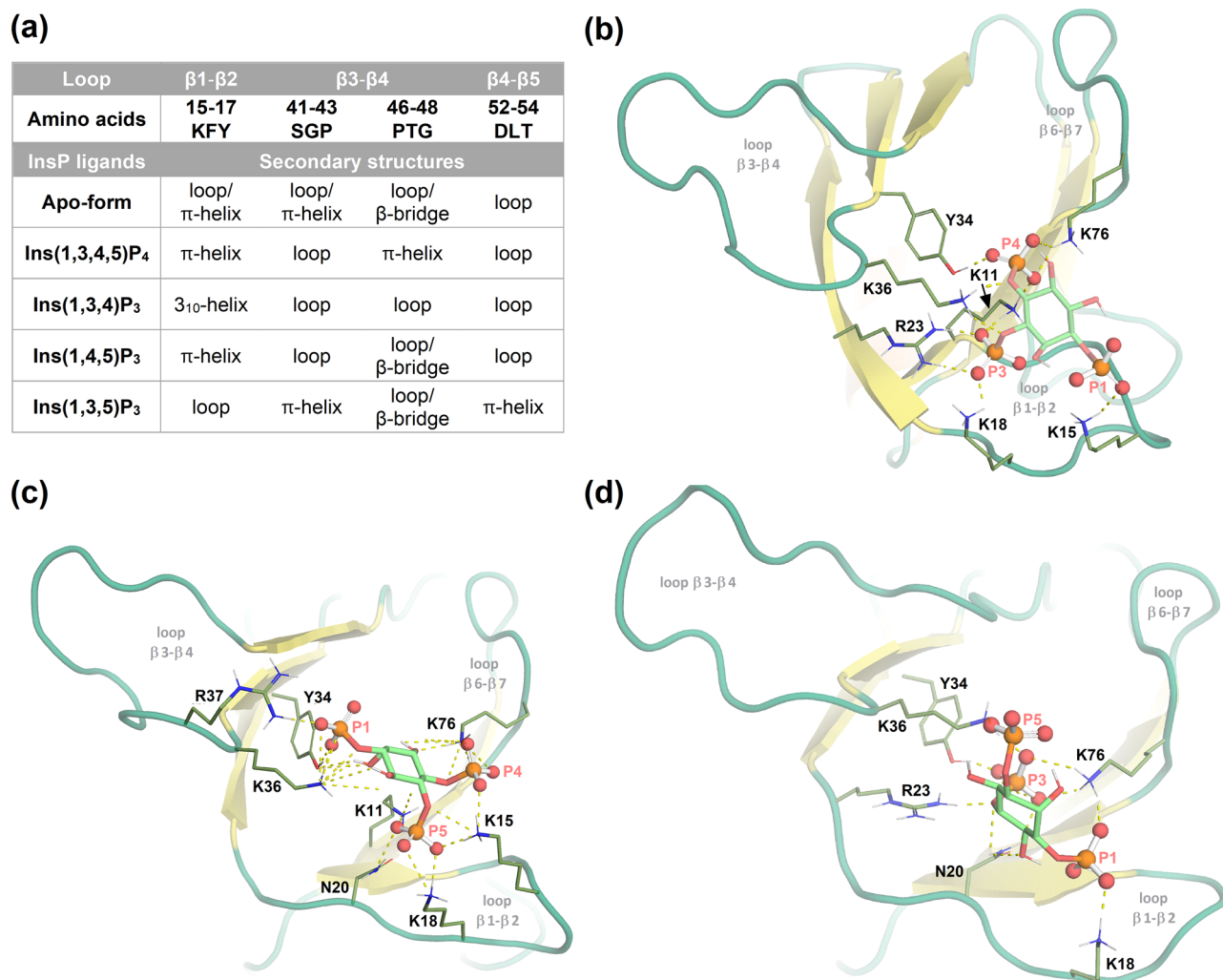


**Figure 5.** Conformational changes of *TcAkt*-PH loop regions induced by binding of different InsP ligands. **(a)** Table of loop-to-helix transitions of *TcAkt*-PH interacting with Ins(1,3,4,5)P<sub>4</sub>, Ins(1,3,4)P<sub>3</sub>, Ins(1,4,5)P<sub>3</sub> or Ins(1,3,5)P<sub>3</sub>. As determined by NMR experiments, strongest binder Ins(1,3,4,5)P<sub>4</sub> stabilizes loop-to- $\pi$ -helix transitions in stretches 15–17 and 46–48 and simultaneously destabilizes region 41–43. Ins(1,3,5)P<sub>3</sub> reduces the  $\pi$ -helix tendency of stretch 15–17 but induces  $\pi$ -helix formation in regions 41–43 and 52–54. Ligands Ins(1,3,4)P<sub>3</sub> and Ins(1,4,5)P<sub>3</sub> induce less conformational changes compared to Ins(1,3,4,5)P<sub>4</sub> and Ins(1,3,5)P<sub>3</sub>, showing a significant impact mainly in region 15–17 of *TcAkt*-PH. Ins(1,4,5)P<sub>3</sub> stabilizes a  $\pi$ -helix in 13–15, similar to Ins(1,3,4,5)P<sub>4</sub>, whereas Ins(1,3,4)P<sub>3</sub> represents the only ligand that induces a  $3_{10}$ -helix formation in stretch 15–17. **(b–d)** MD determined protein–ligand structures of *TcAkt*-PH interacting with **(b)** Ins(1,3,4)P<sub>3</sub>, **(c)** Ins(1,4,5)P<sub>3</sub> and **(d)** Ins(1,3,5)P<sub>3</sub>: Interacting residues are shown in sticks, contacts in dashed yellow lines, phosphate groups in red (ball representation). The presented frames were carefully chosen from the last 1  $\mu$ s MD simulation to showcase the interacting residues adequately.

dependent on Mg<sup>2+</sup> (Figs. S16 and S17). The Mn<sup>2+</sup> binding residues in the crystal structure of *HsAkt2* (N293 and D280) align with the corresponding residues in *TcAkt* (N262 and D275), confirming a conserved binding mechanism of *TcAkt* and *HsAkt* (see SI Section 2).

#### Interdomain interface of *TcAkt* is established via hydrophobic and aromatic interactions

The interface between the kinase and the PH domain represents a favorable target for the inactivation of *HsAkt1* due to its autoinhibitory functionality<sup>25,26,28–30</sup>. To analyze *TcAkt* potential as drug target against CD, a detailed examination of this region is therefore of high interest.

The AF model of full-length *TcAkt* is present in a closed conformation forming interdomain interactions between the *TcAkt*-PH and the kinase domain (Figs. 6 and 8c). The interface between loop  $\beta 1-\beta 2$  of *TcAkt*-PH and the C-lobe of the *TcAkt*-kinase domain is constructed from a network of non-bonded interactions (33 contacts between 20 residues) (Figs. 9d and S18) and has a surface area of 412–460 Å<sup>2</sup>. The tip of loop  $\beta 1-\beta 2$  of *TcAkt*-PH carries two aromatic residues, F16 and Y17, which contribute to the hydrophobic aromatic cluster of the kinase domain built of F289, F291, F302 and Y340 (Figs. 8a, S14, and S19). F16 interacts directly with F291 and Y340, and additionally forms a weak  $\pi$ -stacking interaction with Y340 (ring-to-ring distance 4.2 Å)

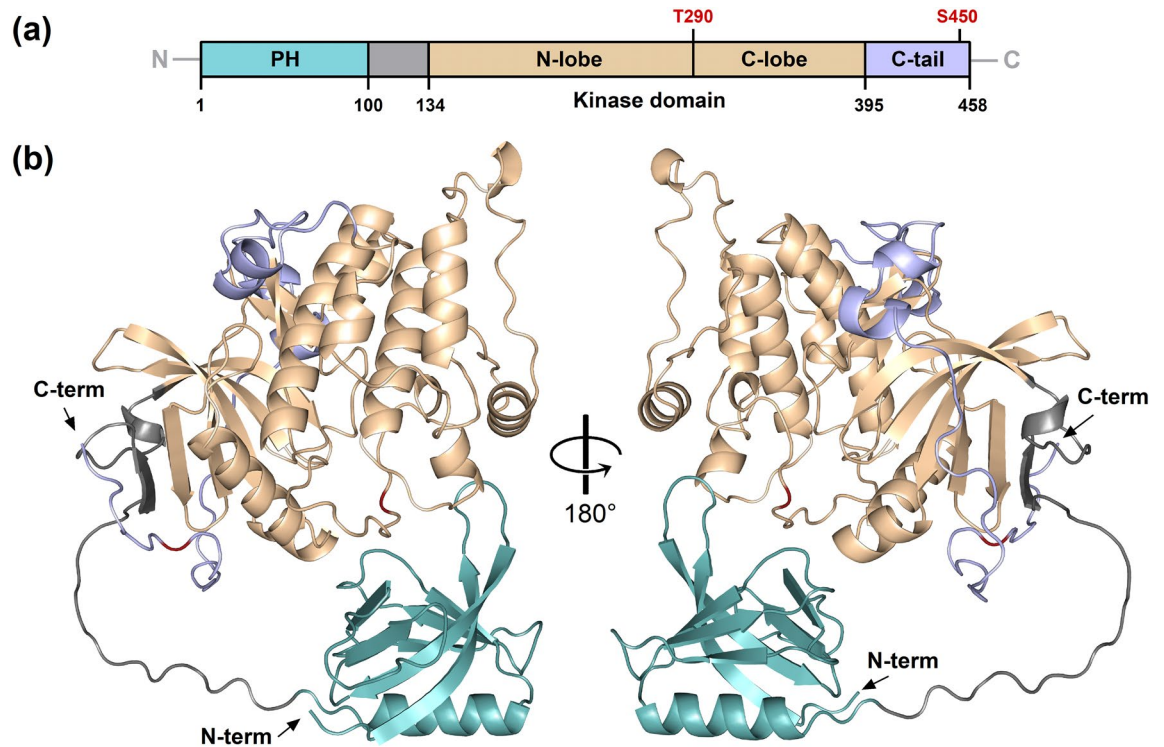


**Figure 6.** AF derived model of full-length *TcAkt*. (a) Schematic representation of *TcAkt* domains: *TcAkt* consists of an N-terminal PH-domain (aa 1–100) (turquoise), a flexible linker (aa 100–134) (grey), a kinase domain divided in a N-lobe and C-lobe (aa 134–395) (sand) and a C-tail (aa 395–458) (lavender). Two putative p-sites are shown in red: T290, S450. (b) Cartoon representation of full-length *TcAkt* model. Same color scheme as in (a).

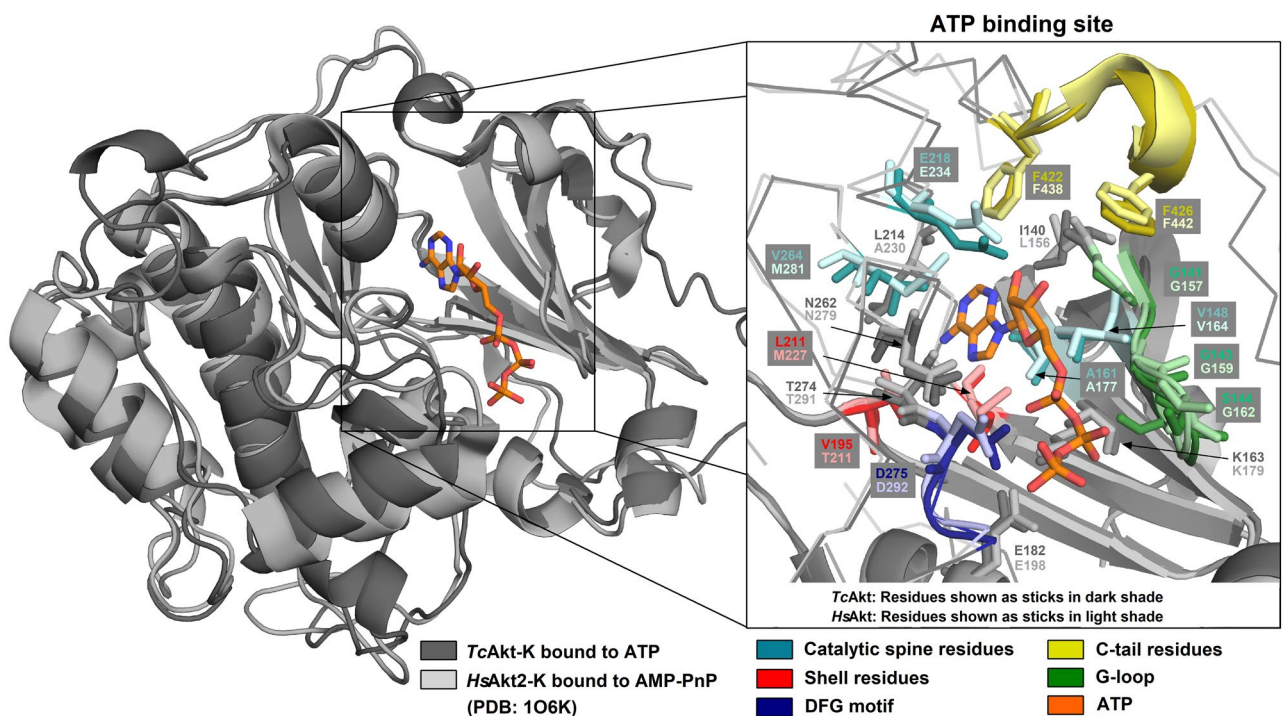


**Figure 7.** ATP bound to *TcAkt* and *HsAkt2* kinase domains. *TcAkt* kinase domain (dark grey) bound to ATP (orange sticks) was calculated with RoseTTAFold<sup>72</sup>. *HsAkt2* kinase domain (light grey) was complexed with ATP analog, AMP-PnP (not shown) (PDB: 1O6K)<sup>73,74</sup> (all-atom RMSD of aligned structures 0.883 Å). Zoomed details show ATP binding site. *TcAkt* residues are shown in dark sticks and *HsAkt* residues are shown in light sticks. Colors refer to specific regions of the kinase domain: Catalytic spine residues (turquoise), shell residues (red), DFG motif (blue), C-tail residues (yellow), G-loop (green), other residues interacting with ATP (grey).

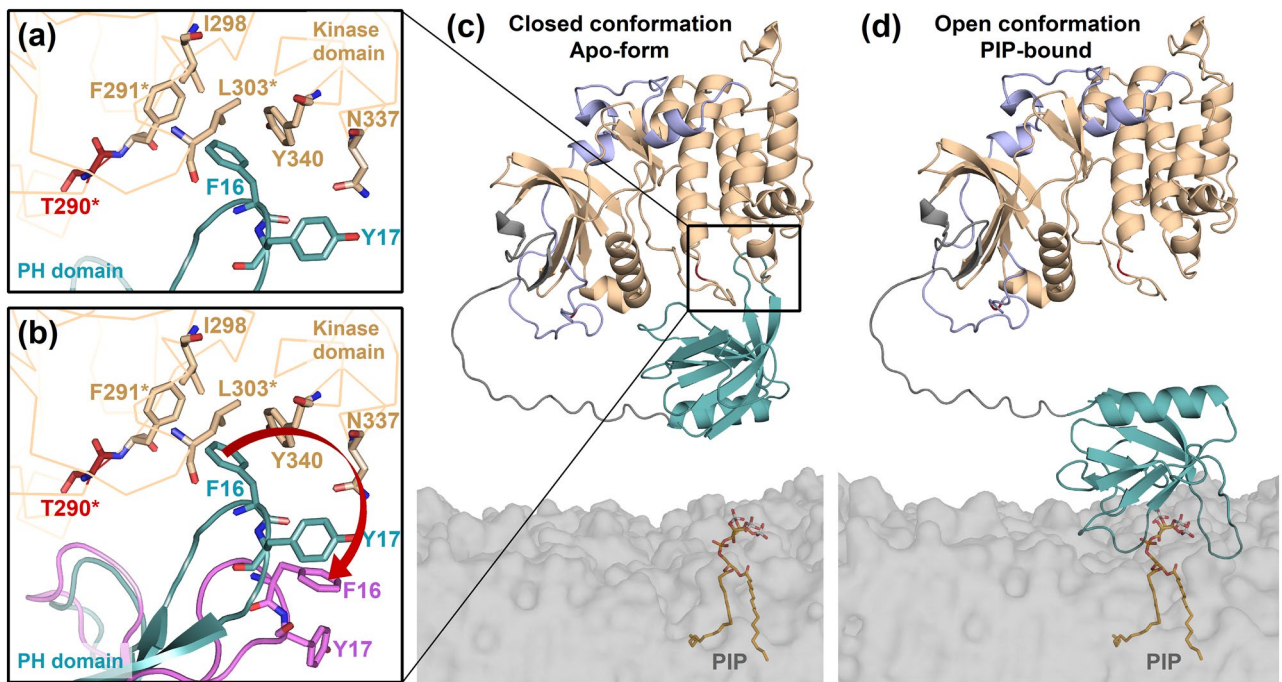


**Figure 8.** Proposed model of *TcAkt* activation via disruption of its autoinhibitory interface upon PIP-binding. *TcAkt* PH domain is shown in turquoise, *TcAkt* kinase domain in sand and the C-tail in lavender. (a) Interdomain contacts between the hydrophobic tip of the PH domain (sticks colored in turquoise) and the kinase domain (sticks colored in sand) are shown as zoomed detail. Phosphorylation site T290 is colored in red. Conserved residues are marked with an asterisk (\*). (b) Ligand induced bending of *TcAkt* loop  $\beta$ 1- $\beta$ 2. Superposition of *TcAkt* apo-form (a) and PIP-bound *TcAkt* determined by MD simulations (pink). Red arrow indicates conformational changes upon binding to PIPs. (c) *TcAkt* is present in a closed conformation (inactive) and gets recruited to the membrane. The PH domain and the kinase domain are interacting via an autoinhibitory interface. (d) The binding of the *TcAkt* PH domain to PIP molecules in the membrane induces conformational changes of the hydrophobic tip (F16, Y17) of the PH domain loop  $\beta$ 1- $\beta$ 2, leading to an opening of the structure and the disruption of the intramolecular autoinhibitory interface including a surface exposure of otherwise buried phosphorylation site T290.

(Fig. S19). The involvement of aromatic residues in the formation of the interdomain interface between loop  $\beta$ 1- $\beta$ 2 of the PH domain and the C-lobe of the kinase domain is also observed in *HsAkt1* (Figs. 9c and S19).

### Model of PH domain-mediated Akt autoinhibition in *T. cruzi*

In *HsAkt1* PIPs recruit the PH domain to the membrane by direct interactions, thus disrupting the autoinhibitory interface between the kinase and the PH domain<sup>25,26,28–30</sup>. This conformational rearrangement exposes the activation loop and the h-motif of the kinase domain, thereby enabling phosphorylation of T308 and S473 and activation of Akt<sup>26,30</sup>. In the absence of PIPs, *HsAkt1* stays in its inactive closed conformation, maintaining the autoinhibitory interface between the kinase and the PH domain<sup>78</sup>.

We propose a similar mechanism of action for *TcAkt*. As shown in the presented AF model, hydrophobic interdomain interactions between the activation loop of the kinase domain and loop  $\beta$ 1- $\beta$ 2 of the PH domain, cause a closed conformation of *TcAkt* (Fig. 8a,c). In this conformation, the putative phosphorylation site of *TcAkt* T290<sup>27</sup> is not accessible, as it is shielded by the PH domain (Figs. 8a and S13). Binding of the *TcAkt*-PH domain to a PIP headgroup induces a bending of loop  $\beta$ 1- $\beta$ 2, as observed by MD simulations (Fig. S11). An opening of loop  $\beta$ 1- $\beta$ 2 involves a change of the position of residue F16, which is thus pulled away from the interdomain interface as shown in Fig. 8b. As a consequence, the hydrophobic cluster of the kinase domain needs to be rearranged to shield the non-polar residues from the solvent exposure. This rearrangement of the region around the activation loop, including T290, could lead to an exposed position of T290, thereby enabling its phosphorylation and consequently the activity enhancement of *TcAkt* (Fig. 8b). The described disruption of the interface is accelerated as residues K76, T47, K15 and K36, previously involved in the interface, are switching interaction partners upon PIP contact (Fig. 8b,d). The disruption of the autoinhibitory interface consequently leads to an open conformation (Fig. 8d) that is associated with activation of Akt.

### The interdomain interface of *TcAkt* differs from *HsAkt*

For evaluation of *TcAkt*'s potential as drug target against CD, it is inevitable to characterize similarities and differences to its human ortholog in order to highlight putative regions for the inhibition of *TcAkt*. The following analysis concentrates on two activity essential regions: the autoinhibitory interface and the PIP binding site, both revealing clear structural and sequential differences between *TcAkt* and *HsAkt1* as shown in Fig. 9.

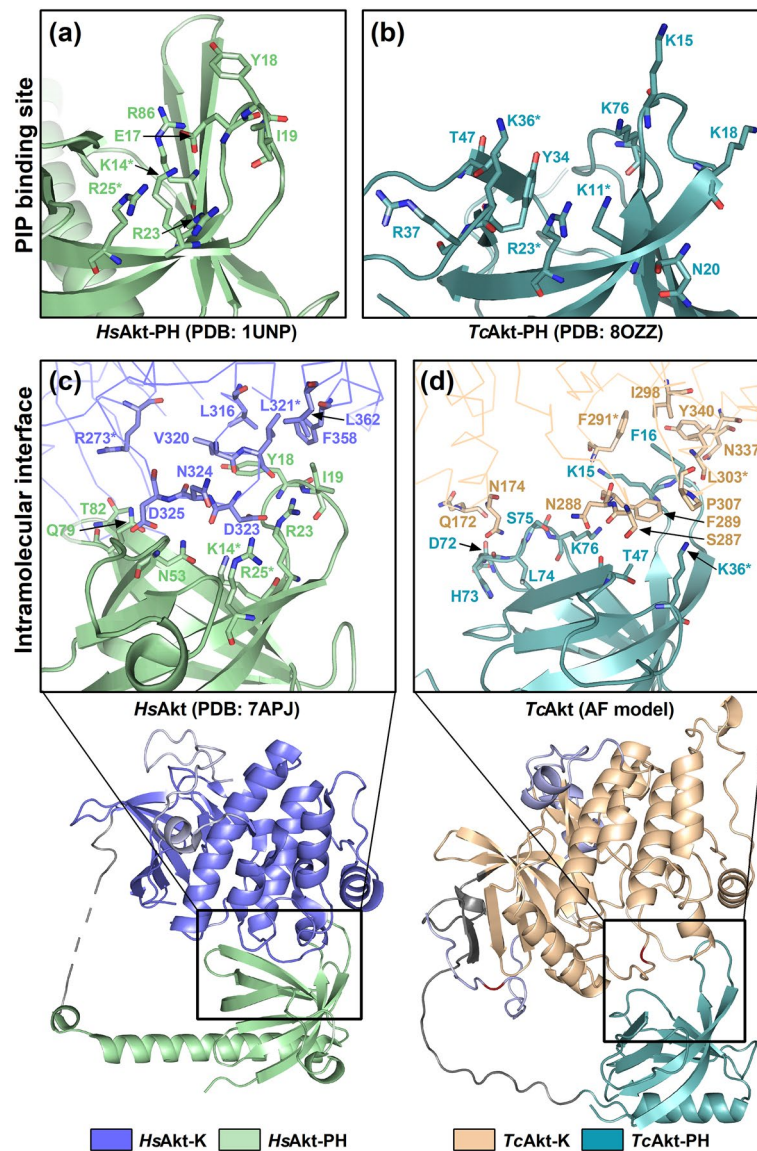


**Figure 9.** Structural analysis of activity essential regions of *TcAkt* and *HsAkt1*. Due to high differences in the residual arrangements the structures are not superimposed. *HsAkt* PH domain is shown in green, *HsAkt* kinase domain in blue and the C-tail in grey. *TcAkt* PH domain is shown in turquoise, *TcAkt* kinase domain in sand and the C-tail in lavender. Flexible interdomain linkers are shown in light grey. PIP binding site: (a) PIP binding site of *HsAkt1*: PIP interacting residues are shown as green sticks (derived from the crystal structure of *HsAkt1*-PH in complex with  $\text{Ins}(1,3,4,5)\text{P}_4$ ; PDB: 1UNQ) and presented on the apo structure (PDB: 1UNP) for comparative reasons. (b) PIP binding site of *TcAkt*: PIP interacting residues are shown as turquoise sticks (derived from NMR analysis and MD simulations) and presented on the apo structure (PDB: 8OZZ). Intramolecular interface: (c) Intramolecular interface of *HsAkt1* as zoomed detail from full-length *HsAkt1* (PDB: 7APJ): Involved residues of the kinase (*HsAkt1*-K: blue) and the PH domain (*HsAkt1*-PH: green) are shown as sticks. (d) Intramolecular interface of *TcAkt* as zoomed detail from full-length *TcAkt* (AF model): Involved residues of the kinase (*HsAkt1*-K: sand) and the PH domain (*HsAkt1*-PH: turquoise) are shown as sticks. Conserved residues are marked with an asterisk (\*).

Overall, the presented AF model of *TcAkt* is in good alignment with the crystal structure of *HsAkt1* (PDB: 7APJ) and the *HsAkt1* AF model (AF-DB: AF-P31749-F1), where loop regions of the kinase domain are visible<sup>25</sup> (Fig. S12a,b). In contrast to the kinase domains which usually share a high conservation, the sequences of PH domains are generally more diverse among different species<sup>45</sup>. The sequence similarity (SS) of full-length sequences of *TcAkt* and *HsAkt1* is 52.6%, while kinase domains share a 64.4% SS and PH domains have a SS of only 36.2% (Fig. S21).

As previously described, the interdomain interface of *TcAkt* represents a promising target for Akt inhibition. As shown in Fig. 9, the structural built of the interdomain interface differs significantly between *HsAkt* and *TcAkt*. Despite the distinctive structural arrangements, the interdomain interface of *TcAkt* and *HsAkt1* is basically

constituted via a hydrophobic interface, including an aromatic cluster (Figs. 9c,d and S19). In both organisms, the hydrophobic tip of loop  $\beta 1$ - $\beta 2$  of the PH domain interacts with hydrophobic residues of the kinase domain (Fig. 9c,d). In *TcAkt*, the hydrophobic tip of  $\beta 1$ - $\beta 2$  in *TcAkt* is formed by residues F16 and Y17, compared to residues Y18 and I19 in *HsAkt1*. In *HsAkt1*, Y18 was stated to form a  $\pi$ -stacking interaction with F309 of the kinase domain<sup>25,29</sup>. In the presented AF model of *TcAkt*, a weak  $\pi$ -stacking interaction is established between F16 and Y340. In *HsAkt1*, functional relevant residues D323 and D325, as well as E17, have been described, which are involved in the interdomain interface<sup>29</sup>. Mentioned residues are not present in *TcAkt*. In *HsAkt1* D323 and D325 form interfacial contacts to the PH domain (loop  $\beta 6$ - $\beta 7$ , loop  $\beta 3$ - $\beta 4$ , strands  $\beta 1$  and  $\beta 2$ ) and mutations result in *HsAkt1* hyperphosphorylation<sup>29</sup>. *HsAkt1* E17 forms a salt bridge with R86 stabilizing the autoinhibitory interface<sup>29</sup>. Oncogenic *HsAkt1* mutant E17K results in enhanced membrane binding<sup>29</sup>. In *TcAkt*, the interdomain interface is not stabilized by salt bridges. *TcAkt* contains K15, at a similar position to *HsAkt1* E17, but forming a hydrogen bond with F291.

### The PIP<sub>3</sub> binding site of *TcAkt* is structurally different to *HsAkt* but is recognized by human PIP<sub>3</sub> competitor PIT-1 due to its basic charge

A putative region for *TcAkt* inhibition represents the PIP binding site which regulates its activity and guides Akt function<sup>42-44</sup>. Despite two conserved basic residues (*Tc*: K11, R23; *Hs*: K14, R25), the binding clefts of *HsAkt1*-PH and *TcAkt*-PH are structurally and sequentially diverse as described in Fig. 9. The proposed consensus sequence KXn(K/R)XR located in loop  $\beta 1$ - $\beta 2$  and strand  $\beta 2$  to predict interactions with PIPs phosphorylated at position 3, matches with *HsAkt1* but not with *TcAkt*<sup>42,46</sup> (Fig. S14). Despite the differences in the amino acid composition of the binding site, the binding mode to PIP ligands is also established in distinctive manners. In mammalian PH domains mainly strands  $\beta 1$  and  $\beta 2$  (including loop  $\beta 1$ - $\beta 2$ ) provide primary contact sites to PIP ligands<sup>45,46</sup>, involving also hydrophobic residues (loop  $\beta 1$ - $\beta 2$ : Y18, I19) (PDB: 1UNQ) (Fig. 9a). In contrast, NMR and MD experiments performed with *TcAkt*-PH reveal strictly polar protein–ligand interactions and furthermore show that besides strands  $\beta 1$  and  $\beta 2$ , also loops  $\beta 3$ - $\beta 4$  and  $\beta 6$ - $\beta 7$  are involved in PIP interaction (Figs. 3, 4, and 5). Interestingly, according to MSA analysis, the PIP binding site also differs among closely related *Trypanosoma* and *Leishmania* species (see SI Section 3, Figs. 10, S22, and S23) proposing that PIP binding mechanisms are species-specific.

PIT-1 is a non-phosphoinositide small molecule antagonist of PIP<sub>3</sub> that shows inhibition of Akt without affecting other PIP<sub>2</sub>-selective PH domains<sup>32,54</sup>. The PIT-1 binding site of human Akt overlaps with the PIP interaction area, involving residues W22, Y26, and N54 (N54 interacts with the phenyl group of PIT-1, W22 and Y26 interact with nitro-group of PIT-1)<sup>54</sup>. Using the presented AF model of *TcAkt*, we initiated docking experiments with human PIP<sub>3</sub> competitor PIT-1 revealing that the inhibitor binds to human and trypanosomal Akt in a similar manner (Fig. 11, see SI Section 4 ‘Docking studies of *TcAkt* and human Akt inhibitors capivasertib and PIT-1’). The overall basic charge of the PIP<sub>3</sub> binding pocket seems to compensate for the sequential and structural differences of the PIP<sub>3</sub> interaction sites of human and trypanosomal Akt.

### General Akt inhibitor capivasertib binds to *TcAkt*

One of the best-studied examples of ATP-competitive Akt inhibitors is capivasertib<sup>55</sup>. Capivasertib is a pyrrolo[2,3-d]pyrimidine derivative that acts as a pan-Akt inhibitor, inhibiting all human Akt isoforms, by binding into the ATP binding site. Only recently, capivasertib was approved by the FDA for breast cancer treatment, being the first ATP-competitive Akt inhibitor on the market<sup>55,56</sup>. Based on the calculated AF structure of *TcAkt*, we generated protein–ligand models of capivasertib to human and trypanosomal Akt using molecular docking approaches (Fig. 12, see SI Section 4 ‘Docking studies of *TcAkt* and human Akt inhibitors capivasertib and PIT-1’). Although binding sites are similar between the proteins, *TcAkt* reveals a strong stereospecificity for (S)-capivasertib over (R)-capivasertib, which is not observed to that extent for *HsAkt* (see SI Section 4). Whereas in *HsAkt* E234, A230 and E228 are most profound residues for interaction with (S)-capivasertib and (R)-capivasertib, in *TcAkt* E218, L214 and D212 are responsible for the inhibitor’s binding (Fig. 12). Further experiments may be needed for evaluating the inhibitory potential of capivasertib on *TcAkt* activity.

### *TcAkt* inhibition by UBMC-4 and UBMC-6 involves the kinase domain

To date, two *TcAkt* inhibitors UBMC-4<sup>23</sup> and UBMC-6<sup>24</sup> have been defined, both detected via virtual screening and molecular docking approaches. Nevertheless, the lack of structural information restricts a detailed understanding of the inhibitory mechanisms. The presented AF-model enables the determination of the binding location of previously described *TcAkt* inhibitors, thus offering insights into their mechanism of action (Fig. 13).

UBMC-4 has been recently described as a potent *TcAkt* inhibitor in *T. cruzi* cell structures, targeting vital cellular processes and resulting in various severe effects, including apoptosis-like events<sup>23</sup>. It furthermore reveals relatively low cytotoxicity on human cell lines (LC50 > 40  $\mu$ M) and effective absorption in mice models<sup>23</sup>. *TcAkt* inhibitor UBMC-4 was assumed to bind to the PH domain according to published MD studies<sup>23</sup>. Nevertheless, combining published data with the presented AF model, localizes the UBMC-4 binding region at the linker region between the PH and the kinase domain (R103, T108) and at the kinase domain (L131, D132, T203, K204, F435) (Fig. 13). The binding position of UBMC-4 suggests that inhibition of *TcAkt* is achieved by restricting the flexibility of the interdomain linker region and thereby preventing PIP induced conformational changes as well as an opening of *TcAkt*.

UBMC-6 represents another putative *TcAkt* inhibitor, having an inhibitory effect on *T. cruzi* amastigotes and was also tested for its toxicity on human monocyte-derived macrophages<sup>24,79</sup>. According to the presented AF structure, UBMC-6 binds close to the h-motif of *TcAkt* and the p-sites T290 and S450 (K128, V129, S130, L131,

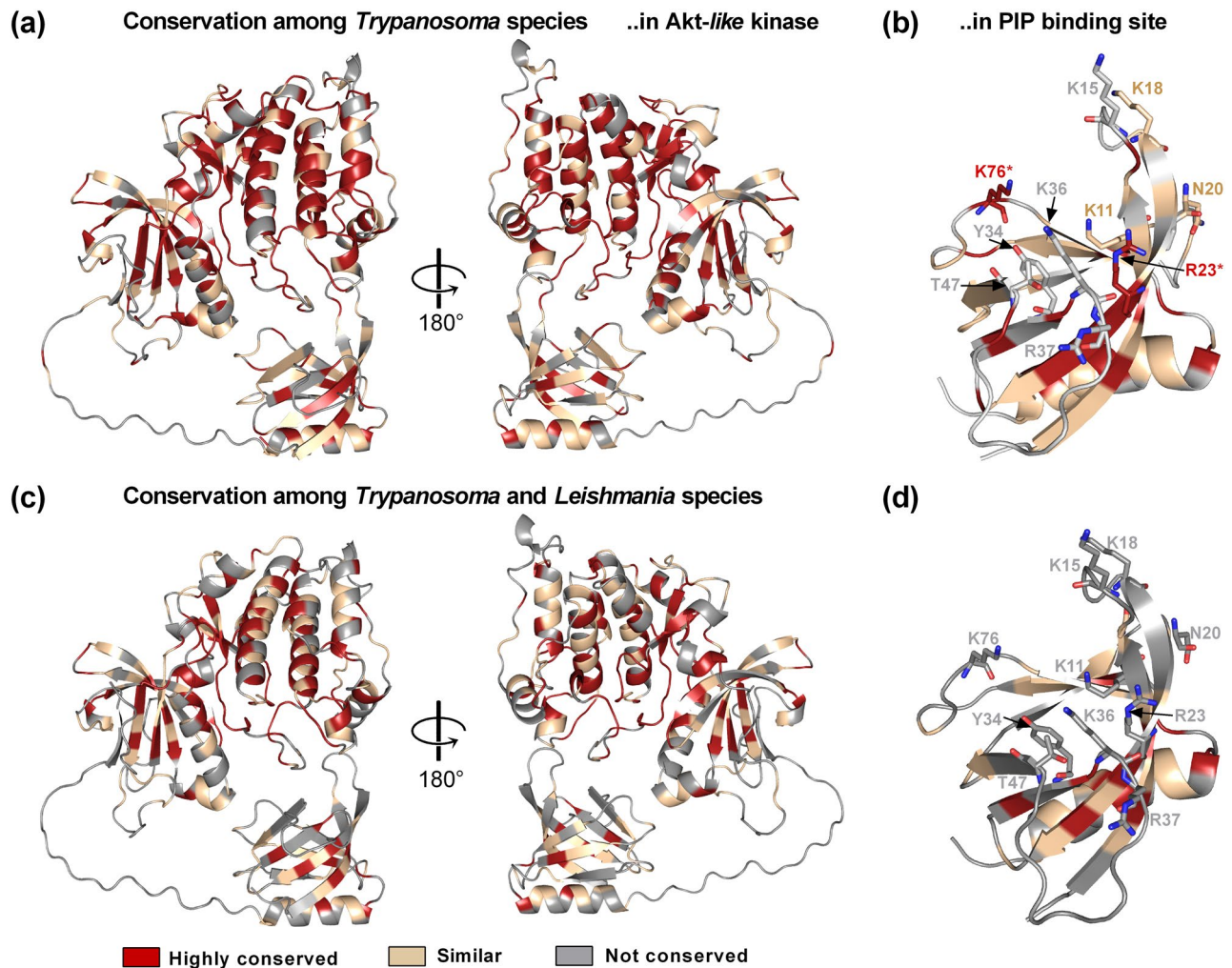


**Figure 10.** MSA derived conserved regions of Akt-like proteins in *Trypanosoma* and *Leishmania* species highlighted on full-length *TcAkt* (MSA: Figs. S22 and S23). Conserved residues are shown in red (in MSA residues are marked with an asterisk (\*)), residues which have similar properties are colored in sand (in MSA residues marked with dots (:,)), non-conserved residues are shown in grey. Residues involved in PIP interaction, are shown as sticks. (a) Conserved regions of Akt-like proteins among *Trypanosoma* spp. (Fig. S22) (b) Conserved residues in PIP binding site among *Trypanosoma* spp. (c) Conserved regions of Akt-like proteins among *Trypanosoma* and *Leishmania* spp. (Fig. S23) (d) Conserved residues in PIP binding sites of *Trypanosoma* spp. and *Leishmania* spp. Further details are described in SI Section 3.

D132, F201, T203, K205, P431, F435, E437), an important region to regulate Akt stability<sup>80</sup>. Likely, UBMC-6 binding blocks the activity essential h-motif and may lead to Akt protein degradation.

## Discussion

The presented NMR structure, in combination with interaction experiments, MD simulations, Molecular Docking and AF-calculations, provides primary insights into the structure and function of a putative target against CD: *TcAkt*. The experiments reveal a PIP binding area, including ligand-induced versatile conformational changes of *TcAkt* regions, which likely guide the broad functionality of this central protein. The experimentally derived information combined with a full-length model of *TcAkt* and sequential analysis exposes activity essential regions of the proteins, leading to a proposed model of *TcAkt* activation via PIP-induced disruption of its interdomain interface. Detailed structural information reveal activity crucial regions of *TcAkt* with clear structural differences to the human ortholog *HsAkt1* and thus highlights putative regions for targeting *TcAkt* inhibition.

## Conformational changes induced by PIP ligands depend on phosphorylation patterns and play a crucial role in Akt activity

*TcAkt* binds PIP headgroups differing in phosphorylation of the inositol ring in the same binding pocket with comparable binding affinities but with clear preferences for P3 and P5 phosphorylations (Fig. S10). Phosphorylation patterns of PIP headgroup inositol rings furthermore induce distinctive patterns of conformational changes, mainly regarding loop regions  $\beta 1$ - $\beta 2$ ,  $\beta 3$ - $\beta 4$  and  $\beta 4$ - $\beta 5$  of *TcAkt*-PH (Figs. 5a, S8, and S9). Nevertheless, all tested

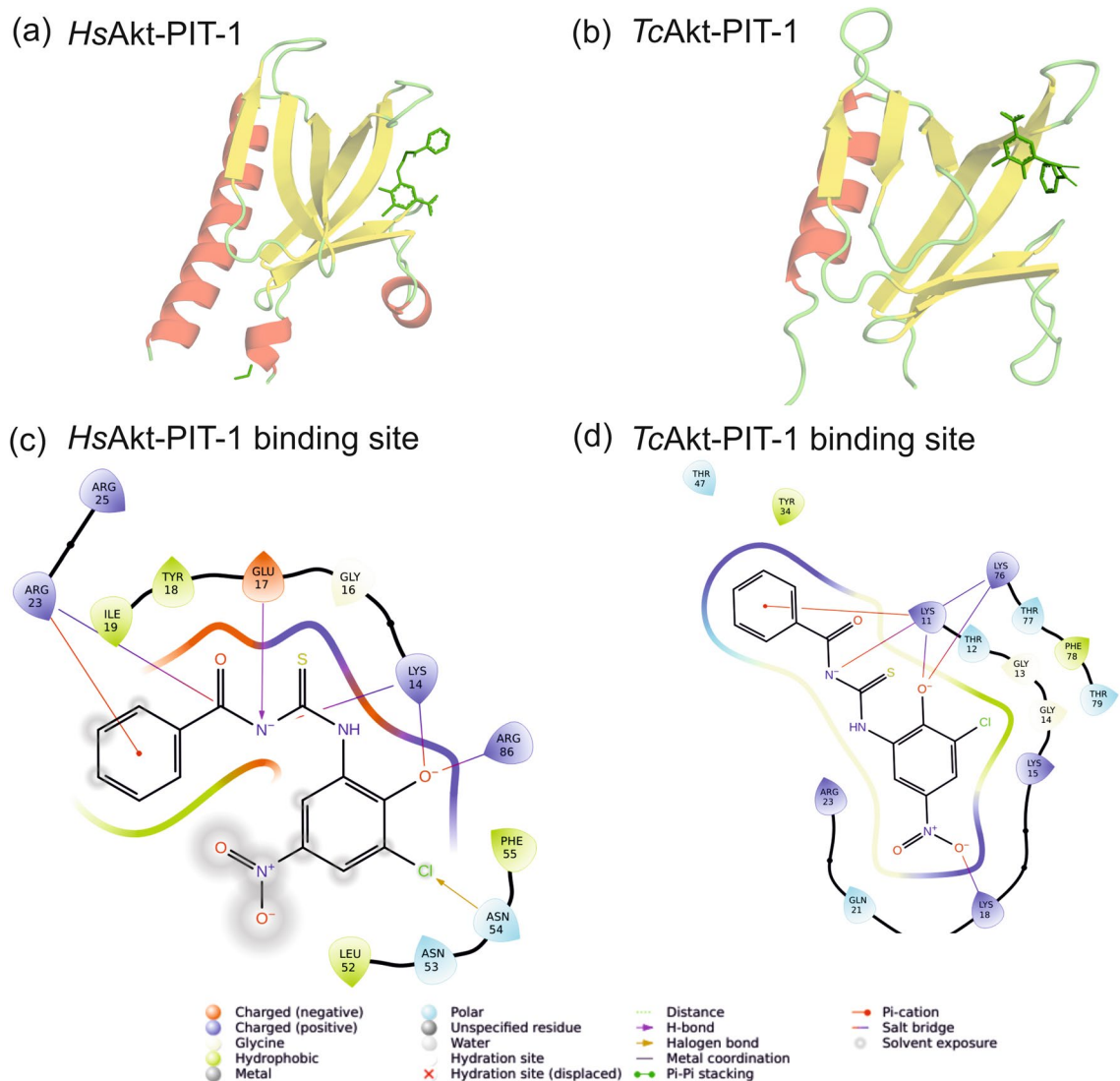


**Figure 11.** Docking studies using human PIP<sub>3</sub> competitor PIT-1 with *HsAkt* and *TcAkt*. Docking derived model of PIT-1 bound to (a) *HsAkt*-PH and (b) *TcAkt*-PH. 2D representation of interacting residues within 4 Å to PIT-1 of (c) *HsAkt* and (d) *TcAkt*. Basic charged residues enable interaction with PIT-1. In *HsAkt* residues K14, R23, and R86 are involved in ionic interactions with PIT-1. In *TcAkt* PIT-1 residues K11, K18 and K76 enable PIT-1 interaction.

PIP headgroups result in an opening of loop  $\beta$ 1- $\beta$ 2 upon binding to the PH domain, potentially inducing the disruption of the autoinhibitory interface (Fig. 8b).

In *HsAkt*1, activation is strictly limited to lipid second messenger molecules PI(3,4,5)P<sub>3</sub> and PI(3,4)P<sub>2</sub>, revealing a different ligand specificity compared to *TcAkt*<sup>26,32,42,64,65,81,82</sup>. In *HsAkt*1, Ins(1,3,4,5)P<sub>4</sub> induces a loop-to-helix transition of residues 44–46 (DVD) located in loop  $\beta$ 3- $\beta$ 4<sup>32,81,83</sup>. Destabilization of the helical formation by mutagenesis (DVD to GPG) consequently resulted in poor kinase activity of S473-phosphorylated Akt, suggesting that dynamics of the DVD motif are essential for the displacement of the PH domain from the kinase domain in response to pS473<sup>28</sup>.

Similarly, Ins(1,3,4,5)P<sub>4</sub> also stabilizes a loop-to-helix transition of residues 41–43 (SGP) in loop  $\beta$ 3- $\beta$ 4 of *TcAkt* (Figs. 5a, S8, and S9). Other tested ligands did not induce these conformational changes. Three of the four tested ligands result in helical conformations of region 15–17 (KPY) located at loop  $\beta$ 1- $\beta$ 2 at the direct binding site of PIP, whereas only Ins(1,3,5)P<sub>3</sub> destabilizes the helix transition. Destabilizing effects of Ins(1,3,5)P<sub>3</sub> lead to increased flexibility, which could enable interactions with other molecules or regulate functionality<sup>84</sup>. Nevertheless, further experiments are needed to determine the exact effect of local conformational changes on the activity of *TcAkt*.

The presented experiments show a complex pattern of diverse stabilizing or destabilizing effects of PIP ligands on *TcAkt*, proposing, similarly to *HsAkt*1, that the dynamics of loop regions of the PH domain are crucial for the functionality of *TcAkt*. Targeting the PIP-affected loop regions via binding of a ligand could offer another possibility for *TcAkt* inactivation by preventing subsequent structural changes essential for activity.

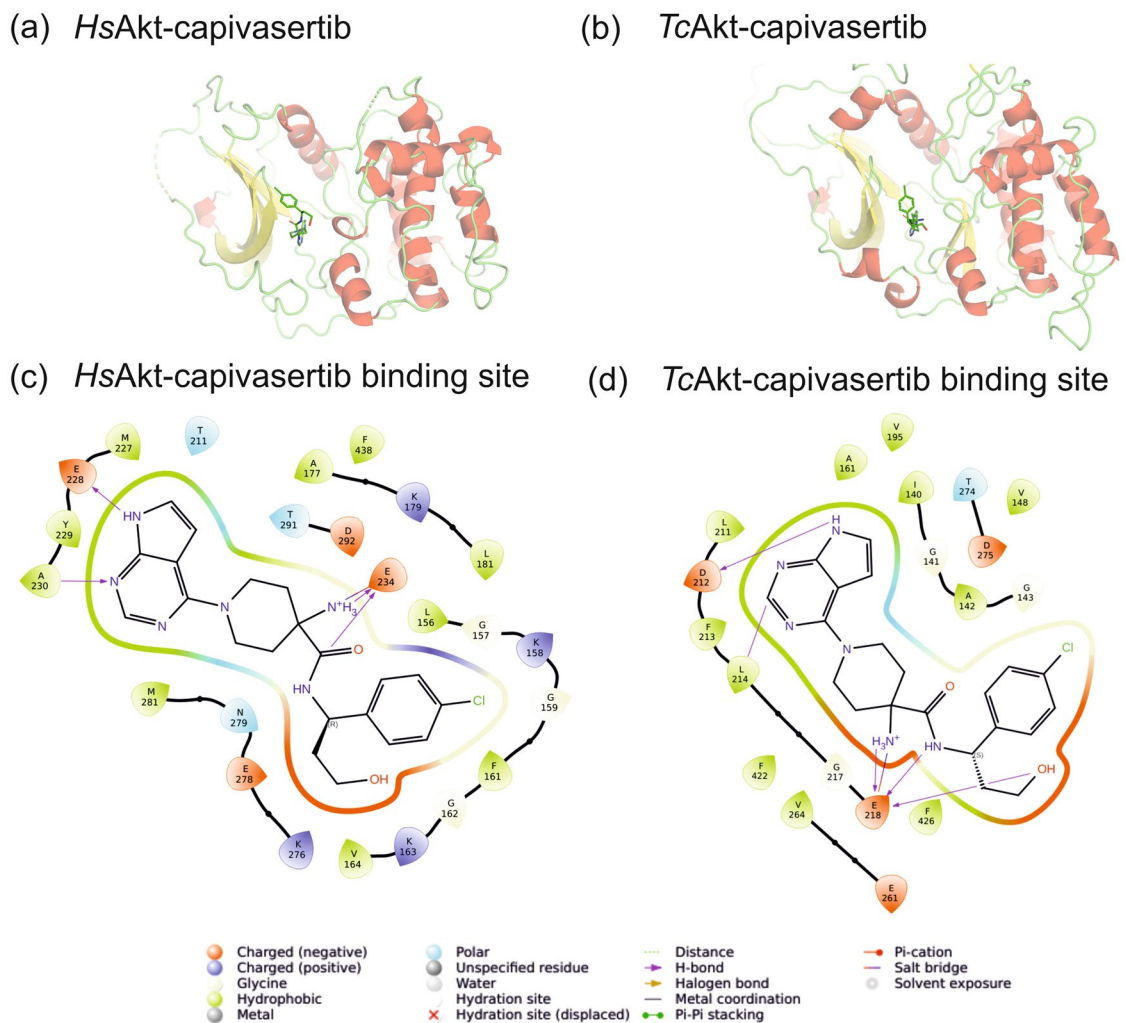


**Figure 12.** Docking studies with human Akt inhibitor capivasertib and *HsAkt* and *TcAkt*. Docking derived model of capivasertib bound to (a) *HsAkt*-K and (b) *TcAkt*-K. 2D representation of interacting residues within 4 Å of capivasertib of (c) *HsAkt*-K and (d) *TcAkt*-K. (see SI Section 4 ‘Docking studies of *TcAkt* and human Akt inhibitors capivasertib and PIT-1’).

### Potential strategies for *TcAkt* inhibition

*HsAkt* has undergone extensive investigation as a therapeutic target in oncology<sup>85</sup> and more recently it has been studied as drug target for treatment of cardiovascular diseases<sup>86</sup>, metabolic syndrome<sup>54</sup>, Parkinson’s disease<sup>87</sup> and schistosomiasis, caused by the parasite *Schistosoma mansoni*<sup>88</sup>. To inhibit Akt kinases, several inhibitors have been developed based on various approaches, which potentially guide the way for *TcAkt* inhibition.

ATP-competitive inhibitors target the active site in the open conformation of Akt kinases<sup>89–92</sup>. However, a high similarity of the ATP-binding site in *TcAkt*, *HsAkt*1 and potentially other AGC family kinases needs to be considered (Fig. 7)<sup>93,94</sup>. Presented docking studies could confirm that ATP-competitive inhibitor capivasertib recognizes human and trypanosomal Akt via similar binding areas (Fig. 12, SI Section 4).

Another target region for Akt inhibition represents the PIP-binding site of the PH domain. Small molecule antagonists of PIP<sub>3</sub> showed activity against PIP<sub>3</sub>-dependent PI3K/Akt signaling<sup>54</sup> supporting that this represents a promising region for Akt inhibition. Although the structure and sequence of the PIP binding region seems to be species-specific (Figs. 5, 9, 10, and 11), the general basic charge of this area may compensate for structural differences as shown by docking experiments with human PIP<sub>3</sub> competitor PIT-1 and human Akt and *TcAkt* (Fig. 11, SI Section 4).

Allosteric inhibitors bind to the inactive closed conformation of Akt by stabilizing the PH-kinase domain interface thus preventing Akt recruitment to the membrane and consequent Akt activation<sup>89,95</sup>. By targeting both domains, allosteric inhibitors reveal a high selectivity also among Akt isoforms<sup>96–98</sup>. Exploiting the presented significant differences between *HsAkt*1 and *TcAkt* interdomain interfaces (Fig. 9), this class holds potential for the development of *TcAkt*-specific inhibitors.

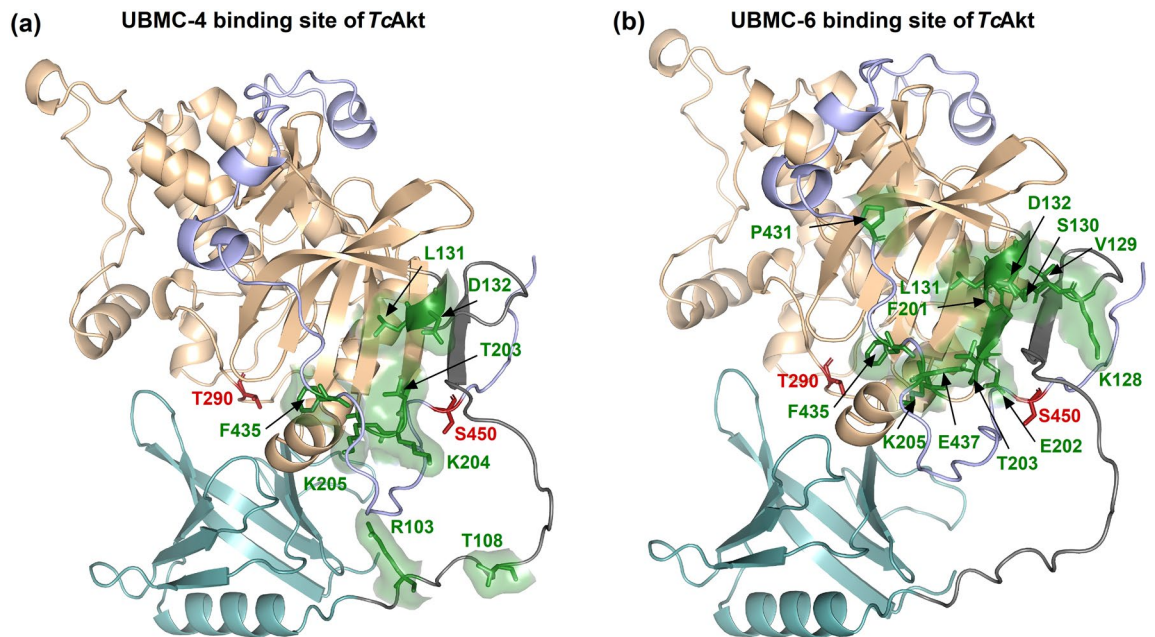


**Figure 13.** *TcAkt* inhibitors UBMC-4 and UBMC-6 binding sites mapped on the AF model of *TcAkt*. *TcAkt* PH domain is shown in turquoise, the flexible linker in grey, the *TcAkt* kinase domain in sand and the C-tail (including the h-motif) in lavender. P-sites are colored in red and shown as sticks. Ligand interacting residues of *TcAkt* are shown in green and presented as sticks. (a) UBMC-4 binding site determined by Bustamante et al.<sup>23</sup> (b) UBMC-6 binding site determined by Ochoa et al.<sup>24</sup>.

## Conclusion

In 2019 the WHO established a ‘World Chagas Disease Day’ on 14<sup>th</sup> of April in order to raise awareness for this neglected tropical disease and its global spread due to factors like climate change. The current lack of safe and efficient treatment in combination with the rising drug resistance of causative protozoan parasite *T. cruzi*, emphasizes the need for new strategies in order to fight this potentially chronic disease. This work offers a detailed analysis of a central protein of *T. cruzi* (Akt-like) as potential drug target against CD and includes atomic resolution data of activity essential regions, thereby forming the basis for structure-based rational drug design.

## Materials and methods

### Chemicals

All reagents were purchased in analytical grade. Ammonium chloride (<sup>15</sup>N, 99%) 98% (CAS 39466-62-1) was purchased from Eurisotop. D-Glucose (U-<sup>13</sup>C<sub>6</sub>, 99%) 98% (CAS 110187-42-3) was purchased from Cambridge Isotope Laboratories, Inc. Inositol 1,3,4,5-tetrakisphosphate >95% (CAS 210488-61-2) was purchased from Echelon Biosciences Inc.

### Constructs

The gene encoding *TcAkt* (TriTrypDB: TcCLB.509047.110, NCBI GeneID: Tc00.1047053509047.110) (1374 bp) originates from the *T. cruzi* CL Brener strain. The sequence is coding for full-length *TcAkt* (52.1 kDa). The *TcAkt* (aa 1–458) and *TcAkt*-PH (aa 1–105) constructs were codon-optimized for *E. coli*, synthesized and inserted into the pET-28a(+) standard vector with a C-terminal 6xHis-tag (see SI Cloning).

### Protein expression and purification

All experiments were performed with *E. coli* BL21(DE3) (Novagen<sup>®</sup>). Plasmids were transformed into BL21 cells by electroporation (1.70 kV, 600 Ohm, 10 μF). Single colonies were selected from agar plates, cultured overnight at 37 °C in 10 mL LB medium containing kanamycin (50 mg/mL) and stored in cryo stocks at –80 °C.

For isotopic labeling, 1000 mL M9 minimal medium (Tables S7 and S8) containing 0.15% <sup>15</sup>N-NH<sub>4</sub>Cl, 0.3% <sup>13</sup>C-Glucose and 50 mg/mL kanamycin were inoculated with the overnight-culture (ONC) and incubated at 37 °C, 180 rpm until the OD<sub>600</sub> reached 0.6–0.8. Induction of protein expression was performed by adding 0.5 mM isopropyl 1-thio-β-D-galactopyranoside (IPTG) and cells were incubated overnight at 25 °C in a baffled shaking flask (180 rpm).

Cells containing *TcAkt*-PH protein were pelleted at 6000 xg, resuspended in 20 mL lysis buffer (50 mM KPi buffer pH 8.0, 10 mM imidazole, 300 mM NaCl) with protease inhibitor (Mix HP, Serva) and disrupted by sonication (45% amplitude, 2 s on, 2 s off) for 15 min on ice. Cell lysates were centrifuged at 4 °C for 1 h at 20,000 xg and the supernatant was loaded onto a pre-equilibrated Ni<sup>2+</sup>-NTA gravity column (Cube Biotech GmbH). The column was washed with 5 column volumes (CV) wash buffer W1 (50 mM KPi pH 8.0, 10 mM imidazole, 1 M NaCl), W2 (50 mM KPi pH 8.0, 20 mM imidazole, 300 mM NaCl) and W3 (50 mM KPi pH 8.0, 35 mM imidazole, 300 mM NaCl), respectively. The elution of His-bound protein was done with 10–12 mL elution

buffer (50 mM KPi pH 8.0, 350 mM imidazole, 300 mM NaCl). The sample was loaded onto a pre-equilibrated size exclusion chromatography (SEC) column (HiLoad 26/600 Superdex 75, GE Healthcare) and the protein was isocratically eluted with SEC buffer (50 mM KPi pH 7.0, 150 mM NaCl, 0.02%  $\text{NaN}_3$ ) into 4 mL fractions. Fractions containing the pure protein were pooled, dialyzed against NMR buffer (50 mM KPi pH 6.5, 100 mM NaCl, 0.02%  $\text{NaN}_3$ ) in 3.5 kDa by dialysis tubes (Spectra/Por, Repligen) and concentrated with ultrafiltration devices (Amicon Ultra, MWCO 3000, Millipore).

Cells containing full-length *TcAkt* protein were pelleted at 6000  $\times g$ , resuspended in 20 mL lysis buffer (50 mM Tris-HCl pH 8.0, 500 mM NaCl) supplemented with protease inhibitor cocktail containing 100 mM PMSF (BioBasic), 100 mM Benzamidine, 0.5 mg/ml Leupeptin, and 70 mg/ml Pepstatin A (BioShop), and sonicated on ice for 4 min (18% amplitude, 60 s on, 60 s off). The mixture was centrifuged at 26,800  $\times g$  at 4 °C for 1 h, and the soluble protein sample was subjected to  $\text{Ni}^{2+}$  affinity chromatography (HisTrap, GE Healthcare Life Sciences). The column was washed with 5%, 7%, and 12% (v/v) imidazole of the elution buffer (50 mM Tris-HCl pH 8.0, 500 mM NaCl, 250 mM imidazole) 5 CV each. The protein was obtained with 100% elution buffer in 1.2 mL fractions. Then, the sample was diluted with 50 mM Tris-HCl pH 8.0 buffer to a final concentration of 125 mM NaCl, filtered using a 0.2  $\mu\text{m}$  filter, and subjected to anion exchange chromatography on a Mono Q<sup>™</sup> 10/100 GL column (Cytiva). The column was pre-equilibrated with buffer (50 mM Tris-HCl pH 8.0, 125 mM NaCl) and the protein was eluted with 500 mM NaCl using a stepwise gradient (125–500 mM) with a flow rate of 1.0 mL/min for 60 min. Pure protein fractions were collected, buffer exchanged (50 mM Tris-HCl pH 8.0, 125 mM NaCl), and concentrated using ultrafiltration devices (Amicon Ultra, MWCO 3000, Millipore). Finally, the concentrated protein fraction was loaded onto the SEC column, pre-equilibrated with buffer (50 mM Tris-HCl pH 8.0, 150 mM NaCl), and protein elution was performed utilizing the same buffer at a flow rate of 0.2 mL/min.

Protein concentration was determined by measuring the absorbance at 280 nm with the specific extinction coefficients for full-length *TcAkt* ( $\epsilon = 55,700 \text{ M}^{-1} \text{ cm}^{-1}$ ) and *TcAkt*-PH ( $\epsilon = 23,900 \text{ M}^{-1} \text{ cm}^{-1}$ ). The purity of the proteins was confirmed by SDS-PAGE, followed by Coomassie blue staining.

### Akt activity assay

The kinase activity of purified recombinant *TcAkt*-6His was measured using a solid phase enzyme-linked immuno-adsorbent assay kit (Abcam, ab139436), according to the manufacturer's instructions. Briefly, 200 ng purified protein was incubated with ATP (1  $\mu\text{g}/\mu\text{l}$ ) for 60 min at 30 °C. The phosphorylation of the synthetic peptide was detected with a phospho-specific substrate antibody incubated 60 min at 21 °C. Subsequently, multiple washes were performed, and anti-rabbit IgG:HRP conjugate (1  $\mu\text{g}/\text{mL}$ ) and TMB substrate were added. The colorimetric detection was measured at 450 nm in a spectrophotometer (Varioskan Flash Multimode Reader, Thermo Scientific). The human *HsAkt3* was used as a positive control and kinase assay dilution buffer was used as blank. Each reaction was performed in triplicate, and the results were expressed as relative kinase activity. Data were analyzed using GraphPad Prism 8.0.1.

### DSF experiments

The  $T_m$  of *TcAkt*-6His was determined by monitoring the fluorescence intensity of SYPRO Orange dye (Thermo Fisher) bound to protein as a function of temperature. The protein was diluted to 1.6  $\mu\text{M}$  in a buffer containing 50 mM Tris-HCl (pH 8.0) and 150 mM NaCl in the presence or absence of the indicated divalent cations (2 mM  $\text{MgCl}_2$  and 2 mM  $\text{MnCl}_2 \cdot 4\text{H}_2\text{O}$ ) with Sypro 5  $\times$  at a final volume of 25  $\mu\text{l}$  into the wells of a 96-well thin wall PCR plate. The nucleotides were evaluated at 16  $\mu\text{M}$ . Thermal scanning (20–95 °C at 1.0 °C/min) was carried out in the real-time PCR equipment (CFX Connect, Biorad) measuring the intensity of fluorescence every 10 s with the SYBR channel. The melting temperature and the first derivative curve were calculated using the software of the equipment. Data are shown as mean from three independent experiments. Reactions without protein, in the presence of reaction buffer, and SYPRO, were included as controls.

### NMR experiments

All spectra were recorded in 3 mm NMR tubes at 25 °C with a 700 MHz Bruker Avance III NMR spectrometer, equipped with a cryogenically cooled 5 mm TCI probe.  $^{13}\text{C}$ -NOESY<sup>99,100</sup>,  $^{13}\text{C}$ -HSQC<sup>101</sup> and HCCH-TOCSY<sup>102–104</sup> were recorded from a 500  $\mu\text{M}$   $^{15}\text{N}$ - and  $^{13}\text{C}$ -labeled sample in 100%  $\text{D}_2\text{O}$ , all other experiments for backbone and side chain assignment were recorded with a 500  $\mu\text{M}$   $^{15}\text{N}$ - and  $^{13}\text{C}$ -labeled sample in 90% NMR buffer (50 mM KPi pH 6.5, 100 mM NaCl, 0.02%  $\text{NaN}_3$ ) and 10% (v/v)  $\text{D}_2\text{O}$ . Spectra were processed with NMRPipe (NMRDraw v5.6 Rev)<sup>105</sup> and analyzed with CcpNmr Analysis 2.4.2.<sup>106</sup>. Molecular images were created with PyMOL (v2.0 Schrödinger, LLC) and UCSF ChimeraX (RBVI)<sup>60</sup>.

### Backbone and side chain assignment

Sequential backbone assignments were determined from the following 3D experiments:  $^{15}\text{N}$ -HSQC<sup>107</sup>, HNCOC<sup>108,109</sup>, HN(CA)CO<sup>109,110</sup>, HNCA<sup>108,109,111</sup>, HN(CO)CA<sup>108,109</sup>, HNCACB<sup>112,113</sup>, HN(CO)CACB<sup>114</sup>, CC(CO)NH<sup>115,116</sup>. For side chain resonance assignments ( $^{13}\text{C}$  and  $^1\text{H}$ ) we used  $^{13}\text{C}$ -HSQC, H(CCO)NH<sup>115,116</sup>, HCCH-TOCSY<sup>102–104</sup> and CC(CO)NH spectra.

### Interproton distance restraints

Interproton distance restraints (NOEs) were obtained from a 3D  $^{15}\text{N}$ -NOESY<sup>99,100,117</sup> (80 ms mixing time) and a 3D  $^{13}\text{C}$ -NOESY (130 ms mixing time) experiment. NOE assignment was achieved by a combination of CYANA-automated NOE assignment<sup>118,119</sup> and manual assignment. Secondary structure predictions were done using backbone assignments and TALOS+<sup>58</sup> (Fig. S24).

### CS-Rosetta structure calculation

For the CS-Rosetta fragment generation we used the provided CS-Rosetta server as described by Shen et al.<sup>57</sup> using the following input parameters: backbone chemical shifts (C $\alpha$ , C $\beta$ , C', H $\alpha$  and HN), TALOS+ restraints<sup>58</sup> and NOEs between the following protons: HN-HN, H $\alpha$ -HN and H $\alpha$ -H $\alpha$  (82 NOEs, including 26 long-range NOEs:  $i-i+(10-100)$ ) (Table S1). Using TALOS+ predictions, the flexible termini were excluded from the subsequent calculations of TcAkt-PH (aa 2–105) (Fig. S24). For the structure generation we used an installed version of Rosetta 3.13<sup>57,58</sup> and additionally included side chain NOEs (59 NOEs including 50 long-range NOEs:  $i-i+(10-100)$ ) (Table S2). 10 000 structures were calculated. The output was validated by plotting the C $\alpha$ -RMSD of each structure to the lowest-energy structure (S\_07667), against the all-atom energy of each structure (Fig. 1a). The plot reveals a clear funnel towards the lowest-energy model, thereby indicating that the CS-Rosetta structure calculation is converged. Ten structures were selected according to the lowest C $\alpha$ -RMSD to the lowest-energy structure resulting in an averaged C $\alpha$ -RMSD value of 1.7 Å, additionally confirming successful structure calculation. Refinement statistics were determined via the PSVS server (PMID: 17186527) (Table S3). The best-scored model (S\_07667) was used for further structural analysis.

### Calculation of electrostatic surface

The coulombic electrostatic potential was calculated from atomic partial charges and coordinates according to Coulomb's law:

$$\varphi = \sum [q_i/\epsilon d_i] \quad (1)$$

$\varphi$ ... potential,  $q_i$ ...atomic partial charges,  $d_i$ ...distances from the atoms,  $\epsilon$ ...dielectric constant.

The resulting potential is in units of kcal/(mol·e) at 298 K. Standard amino acids are assigned atomic partial charges and types from the recommended force field versions in AmberTools 20 (for proteins: ff14SB)<sup>61,62</sup>.

### NMR relaxation experiments

<sup>15</sup>N T1 spin–lattice relaxation times were determined from an inversion recovery experiment (Bruker pulse sequence: hsqct1etf3gpsi3d.2) with delay times of 0.05, 0.1, 0.2, 0.3, 0.4, 0.5, 0.6, 0.7, 0.8, 1.0, 1.5, 2.0, 3.0 and 3.5 s. <sup>15</sup>N T2 spin–spin relaxation times were determined from a spin echo CPMG experiment (Bruker pulse sequence: hsqct2etf3gpsi3d) with delay times of 0.017, 0.034, 0.051, 0.068, 0.085, 0.102, 0.119, 0.136, 0.153, 0.170, 0.187, 0.204, 0.237 and 0.330 s. Spectra were analyzed using CcpNmr Analysis 2.4.2.<sup>106</sup>. The rotational correlation times  $\tau_C$  were calculated for each residue from Eq. (2) (Fig. S2b) and the mean value was calculated:

$$\tau_C \approx \frac{1}{4\pi\nu_N} \sqrt{6 \frac{T_1}{T_2} - 7} \quad (2)$$

$\tau_C$ ...rotational correlation time [s],  $\nu_N$ ...<sup>15</sup>N resonance frequency [Hz],  $T_1$ ...T1 relaxation time [s],  $T_2$ ...T2 relaxation time [s].

HetNOE values were measured with the pulse sequence hsqcnoef3gpsi. Spectra were analyzed using CcpNmr Analysis 2.4.2.<sup>106</sup>. HetNOE values were determined from the measured intensities of a saturated <sup>15</sup>N-HSQC spectrum relative to a reference spectrum:

$$\text{NOE}_{\text{het}} = \left( \frac{I_{\text{sat}}}{I_{\text{ref}}} \right) - 1 \quad (3)$$

$\text{NOE}_{\text{het}}$ ...{<sup>1</sup>H}-<sup>15</sup>N heteronuclear NOE,  $I_{\text{sat}}$ ...Intensities of saturated spectrum,  $I_{\text{ref}}$ ...Intensities of reference spectrum.

### NMR CSP experiments

For CSP experiments, a 170  $\mu\text{M}$  <sup>15</sup>N-labeled sample and a 30 mM stock of Ins(1,3,4,5)P<sub>4</sub> in NMR buffer were prepared. Small volumes of Ins(1,3,4,5)P<sub>4</sub> were added stepwise to the protein sample up to a ratio of 1:35 (protein:ligand). <sup>15</sup>N-HSQC spectra were recorded after each step to follow the shift changes. Spectra were analyzed using CcpNmr Analysis 2.4.2.<sup>106</sup>.

Euclidean distances, also called  $d$ -values, were calculated as described by Williamson<sup>53</sup>:

$$d = \sqrt{\frac{1}{2} [\delta_H^2 + (\alpha * \delta_N)^2]} \quad (4)$$

$d$ ...Euclidean distance,  $\delta_N$ ...<sup>15</sup>N chemical shift changes,  $\delta_H$ ...<sup>1</sup>H chemical shift changes,  $\alpha$ ...scaling factor (glycines  $\alpha=0.2$ , all other amino acids  $\alpha=0.14$ ).

A threshold value was determined according to the procedure described by Schumann et al.<sup>120</sup> to exclude residues with very small shift changes.

The <sup>15</sup>N chemical shifts were weighted with a scaling factor  $\alpha=0.14$ . The dissociation constant ( $K_d$ ) was then fitted for each amino acid individually with the following equation:

$$\Delta\delta_{\text{obs}} = \Delta\delta_{\text{max}} \left\{ \frac{([P]_t + [L]_t + K_d) - \sqrt{([P]_t + [L]_t + K_d)^2 - 4[P]_t[L]_t}}{2[P]_t} \right\} \quad (5)$$

$\Delta\delta_{\text{obs}}$ ...change in observed shift,  $\Delta\delta_{\text{max}}$ ...maximum shift change on saturation,  $[P]_t$ ...total protein concentration,  $[L]_t$ ...total ligand concentration,  $K_d$ ...dissociation constant.

$K_d$  values with  $d$ -values below the calculated threshold ( $d$ -value < 0.008) were excluded from the dataset. Outliers were identified via boxplot analysis and excluded from the dataset ( $K_d > 90 \mu\text{M}$ ). Mean and standard deviation were calculated from the resulting 64 values (Table S4).

### MD simulations

To model the *TcAkt*-PH structure with ligands (Ins(1,3,4,5) $P_4$ , Ins(1,4,5) $P_3$ , Ins(1,3,4) $P_3$ , Ins(1,3,5) $P_3$ ), we have used the experimental structure of the PH domain of *HsAkt* (PDB: 1UNQ) with bound Ins(1,3,4,5) $P_4$  as a template. The coordinates of the *TcAkt*-PH structure were aligned with the *HsAkt*-PH structure. Subsequently, using the builder tool in Maestro (Schrödinger, LLC)<sup>121</sup>, we have utilized the coordinates of the bound ligand to manipulate the structure of the original ligand and model other ligands with the aligned structure of *TcAkt*-PH. Subsequently, hydrogen atoms were added using the protein preparation wizard<sup>122</sup> in Maestro. Each modeled *TcAkt*-PH structure without ligands and with ligands then undergoes an energy minimization step only for the H atom, followed by solvation and neutralization.

For equilibration, the system was subjected to 100 ps of Brownian Dynamics NVT at 10 K with restraints on solute-heavy atoms, followed by short 12 ps NVT and 12 ps NPT at 10 K with restraints on solute-heavy atoms. Later, the temperature was increased to 300 K for another 12 ps NPT run with restraints on solute-heavy atoms. Finally, all restraints were removed, and a short 24 ps NPT run was performed, followed by another 1  $\mu\text{s}$  long NPT at 300 K.

The equilibrated system was then further simulated for 1  $\mu\text{s}$  long production runs at 300 K. In total, each system was simulated for 2  $\mu\text{s}$ . For these simulations, the program Desmond<sup>123</sup> was used with the OPLS4<sup>124</sup> all-atom forcefield. A time step of 2 fs was used throughout the simulations, employing a Nose–Hoover<sup>125,126</sup> thermostat and a Martyna–Tobias–Klein<sup>127</sup> barostat, with relaxation times of 1.0 and 2.0 ps, respectively. The particle mesh Ewald<sup>128</sup> method was used to treat long-range interactions, and a nonbonded cutoff of 9.0 Å was used for short-range interactions. For analysis, the last 1  $\mu\text{s}$  production run has been used.

### AF calculations

*Ab-initio* models for *TcAkt* were calculated using an AlphaFold 2.3 installation in standard configuration for monomers with full databases and monomer model weights<sup>69</sup>. With the full-length sequence (aa 1–458) as input, 25 models were generated and ranked by the highest pTM score. The top-ranked model (see Fig. 6) reached a pTM score of 80.6.

### RoseTTAFold All-Atom assembly calculation

The models of the *TcAkt* kinase domain bound to ATP were calculated on a RoseTTAFold All-Atom<sup>72</sup> installation in standard configuration. A set of 5 models was generated with the domain sequence (331 aa) and the chemical structure of ATP as input. All 5 predicted models show ATP at the same binding site. The models were ranked by the lowest pae\_inter score, the top-ranked model reached a score of 7.6. The models were relaxed using amber99sb<sup>129</sup> and GAFF<sup>130</sup> force fields with parameters oriented to the relaxation algorithm of AlphaFold-Multimer<sup>69,131</sup>. The highest ranked model is shown in Fig. 7.

### Molecular docking

The structure of *HsAkt* was retrieved from the RCSB PDB under accession code 4GV1<sup>55</sup>. Non-protein atoms were then removed from the structure, leaving only the bound inhibitor, Capivasertib. Subsequently, protein preparation was conducted using Maestro<sup>121</sup> which involved the addition of hydrogen atoms following an energy minimization process to refine the positions of the added hydrogen atoms. The coordinates of a modeled *TcAkt* structure were aligned with those of the 4GV1 structure, utilizing the bound inhibitor's coordinates for grid generation. A receptor grid was generated around the bound inhibitor to facilitate docking. The inhibitor molecule underwent a separate ligand preparation step to explore its possible conformations and stereoisomers. Generated ligand conformations were then subjected to docking into the receptor using the extra precision protocol of Glide software<sup>132</sup>. Furthermore, a similar procedure was repeated for docking the PIT-1 (CAS 53501-41-0) inhibitor with the PH-domain of *HsAkt*, employing both the PDB:1UNQ structure and the PH domain of the AF structure of *TcAkt*.

### Data availability

The NMR solution structure of *TcAkt*-PH has been deposited in the PDB with ID 8OZZ. NMR chemical shift assignments have been deposited in the BMRB data bank with accession number 52088. Most data generated and/or analyzed during the current study are included in this article and its supplementary information files. Corresponding raw data tables are available upon request to the corresponding authors.

Received: 19 January 2024; Accepted: 12 April 2024

Published online: 02 May 2024

### References

1. World Health Organization. Chagas disease (also known as American trypanosomiasis). [https://www.who.int/news-room/fact-sheets/detail/chagas-disease-\(american-trypanosomiasis\)](https://www.who.int/news-room/fact-sheets/detail/chagas-disease-(american-trypanosomiasis)) (2023).
2. Martín-Escobano, J. *et al.* An updated view of the *Trypanosoma cruzi* life cycle: Intervention points for an effective treatment. *ACS Infect. Dis.* **8**, 1107–1115 (2022).

3. Abras, A. *et al.* Worldwide control and management of Chagas disease in a new era of globalization: A close look at congenital *Trypanosoma cruzi* infection. *Clin. Microbiol. Rev.* **35**, 1–33 (2022).
4. Alonso-Padilla, J., Pinazo, M. J. & Gascón, J. Chagas disease in Europe. In *Chagas Disease* (eds Altcheh, J. & Freilij, H.) 111–123 (Springer, 2019).
5. Eberhard, F. E., Cunze, S., Kochmann, J. & Klimpel, S. Modelling the climatic suitability of Chagas disease vectors on a global scale. *Elife* **9**, 1–16 (2020).
6. Garza, M. *et al.* Projected future distributions of vectors of *Trypanosoma cruzi* in North America under climate change scenarios. *PLoS Negl. Trop. Dis.* **8**, e2818 (2014).
7. Coura, J. R. The main sceneries of Chagas disease transmission. The vectors, blood and oral transmissions: A comprehensive review. *Mem. Inst. Oswaldo Cruz* **110**, 277–282 (2015).
8. Beatty, N. L., Forsyth, C. J., Burkett-Cadena, N. & Wisely, S. M. Our current understanding of Chagas disease and *Trypanosoma cruzi* infection in the state of Florida: An update on research in this region of the USA. *Curr. Trop. Med. Rep.* **9**, 150–159 (2022).
9. Lascano, F., García Bournissen, F. & Altcheh, J. Review of pharmacological options for the treatment of Chagas disease. *Br. J. Clin. Pharmacol.* **88**, 383–402 (2022).
10. Pérez-Molina, J. A. & Molina, I. Chagas disease. *Lancet* **391**, 82–94 (2018).
11. Apt, W. *Treatment of Chagas Disease. American Trypanosomiasis Chagas Disease: One Hundred Years of Research* 2nd edn. (Elsevier Inc., 2017). <https://doi.org/10.1016/B978-0-12-801029-7.00032-0>.
12. Linciano, P. *et al.* Aryl thiosemicarbazones for the treatment of trypanosomatid infections. *Eur. J. Med. Chem.* **146**, 423–434 (2018).
13. de Barros Dias, M. C. H. *et al.* 1,3-Thiazole derivatives as privileged structures for anti-*Trypanosoma cruzi* activity: Rational design, synthesis, in silico and in vitro studies. *Eur. J. Med. Chem.* **257**, 115508 (2023).
14. Castro Fernandes Melo Reis, R. *et al.* Design and synthesis of new 1,2,3-triazoles derived from eugenol and analogues with in vitro and in vivo activity against *Trypanosoma cruzi*. *Eur. J. Med. Chem.* **258**, 115622 (2023).
15. García-Huertas, P. & Cardona-Castro, N. Advances in the treatment of Chagas disease: Promising new drugs, plants and targets. *Biomed. Pharmacother.* **142**, 112020 (2021).
16. Hargrove, T. Y. *et al.* Complexes of *Trypanosoma cruzi* sterol 14 $\alpha$ -demethylase (CYP51) with two pyridine-based drug candidates for Chagas disease: Structural basis for pathogen selectivity. *J. Biol. Chem.* **288**, 31602–31615 (2013).
17. Doyle, P. S. *et al.* A nonazole CYP51 inhibitor cures Chagas' disease in a mouse model of acute infection. *Antimicrob. Agents Chemother.* **54**, 2480–2488 (2010).
18. Beltran-Hortelano, I., Perez-Silanes, S. & Galiano, S. Trypanothione reductase and superoxide dismutase as current drug targets for *Trypanosoma cruzi*: An overview of compounds with activity against Chagas disease. *Curr. Med. Chem.* **24**, 1066–1138 (2017).
19. de Oliveira, R. G., Cruz, L. R., Mollo, M. C., Dias, L. C. & Kratz, J. M. Chagas disease drug discovery in Latin America: A mini review of antiparasitic agents explored between 2010 and 2021. *Front. Chem.* **9**, 1–7 (2021).
20. Padilla, A. M. *et al.* Discovery of an orally active benzoxaborole prodrug effective in the treatment of Chagas disease in non-human primates. *Nat. Microbiol.* **7**, 1536–1546 (2022).
21. Tarleton, R. L. Effective drug discovery in Chagas disease. *Trends Parasitol.* **39**, 423–431 (2023).
22. De Rycker, M., Wyllie, S., Horn, D., Read, K. D. & Gilbert, I. H. Anti-trypanosomatid drug discovery: progress and challenges. *Nat. Rev. Microbiol.* **21**, 35–50 (2023).
23. Bustamante, C. *et al.* In silico, in vitro, and pharmacokinetic studies of UBMC-4, a potential novel compound for treating against *Trypanosoma cruzi*. *Pathogens* **11**, 616 (2022).
24. Ochoa, R., Rocha-Roa, C., Marin-Villa, M., Robledo, S. M. & Varela-M, R. E. Search of allosteric inhibitors and associated proteins of an AKT-like kinase from *trypanosoma cruzi*. *Int. J. Mol. Sci.* **19**, 3951 (2018).
25. Bae, H. *et al.* PH domain-mediated autoinhibition and oncogenic activation of Akt. *Elife* **11**, 1–27 (2022).
26. Ebner, M., Lučić, I., Leonard, T. A. & Yudushkin, I. PI(3,4,5)P<sub>3</sub> engagement restricts Akt activity to cellular membranes. *Mol. Cell* **65**, 416–431.e6 (2017).
27. Varela, R. E. M., Ochoa, R., Muskus, C. E., Muro, A. & Mollinedo, F. Identification of a RAC/AKT-like gene in *Leishmania* parasites as a putative therapeutic target in leishmaniasis. *Parasites and Vectors* **10**, 1–10 (2017).
28. Chu, N. *et al.* The structural determinants of Ph domain-mediated regulation of Akt revealed by segmental labeling. *Elife* **9**, 1–23 (2020).
29. Truebestein, L. *et al.* Structure of autoinhibited Akt1 reveals mechanism of PIP<sub>3</sub>-mediated activation. *Proc. Natl. Acad. Sci. U. S. A.* **118**, 1–11 (2021).
30. Shaw, A. L. *et al.* ATP-competitive and allosteric inhibitors induce differential conformational changes at the autoinhibitory interface of Akt1. *Structure* **31**, 343–354.e3 (2023).
31. Lučić, I. *et al.* Conformational sampling of membranes by Akt controls its activation and inactivation. *Proc. Natl. Acad. Sci. U. S. A.* **115**, E3940–E3949 (2018).
32. Meuillet, E. J. Novel inhibitors of AKT: Assessment of a different approach targeting the pleckstrin homology domain. *Curr. Med. Chem.* **18**, 2727–2742 (2011).
33. Lu, S. *et al.* The mechanism of ATP-dependent allosteric protection of Akt kinase phosphorylation. *Structure* **23**, 1725–1734 (2015).
34. Modi, V. & Dunbrack, R. L. Defining a new nomenclature for the structures of active and inactive kinases. *Proc. Natl. Acad. Sci. USA* **116**, 6818–6827 (2019).
35. Li, X. *et al.* Autophosphorylation of Akt at threonine 72 and serine 246: A potential mechanism of regulation of Akt kinase activity. *J. Biol. Chem.* **281**, 13837–13843 (2006).
36. Manning, B. D. & Toker, A. AKT/PKB signaling: Navigating the network. *Cell* **169**, 381–405 (2017).
37. Nakayasu, E. S., Gaynor, M. R., Sobreira, T. J. P., Ross, J. A. & Almeida, I. C. Phosphoproteomic analysis of the human pathogen *Trypanosoma cruzi* at the epimastigote stage. *Proteomics* **9**, 3489–3506 (2009).
38. Zhang, H. *et al.* Phosphoprotein analysis using antibodies broadly reactive against phosphorylated motifs. *J. Biol. Chem.* **277**, 39379–39387 (2002).
39. Huang, Q. *et al.* Akt2 kinase suppresses glyceraldehyde-3-phosphate dehydrogenase (GAPDH)-mediated apoptosis in ovarian cancer cells via phosphorylating gapdh at threonine 237 and decreasing its nuclear translocation. *J. Biol. Chem.* **286**, 42211–42220 (2011).
40. Hermida, M. A., Dinesh Kumar, J. & Leslie, N. R. GSK3 and its interactions with the PI3K/AKT/mTOR signalling network. *Adv. Biol. Regul.* **65**, 5–15 (2017).
41. Souza, D. H. F. *et al.* *Trypanosoma cruzi* glycosomal glyceraldehyde-3-phosphate dehydrogenase: Structure, catalytic mechanism and targeted inhibitor design. *FEBS Lett.* **424**, 131–135 (1998).
42. Ferguson, K. M. *et al.* Structural basis for discrimination of 3-phosphoinositides by pleckstrin homology domains. *Mol. Cell* **6**, 373–384 (2000).
43. Vanhaesebroeck, B., Guillermet-Guibert, J., Graupera, M. & Bilanges, B. The emerging mechanisms of isoform-specific PI3K signalling. *Nat. Rev. Mol. Cell Biol.* **11**, 329–341 (2010).
44. Booth, L. A. & Smith, T. K. Lipid metabolism in *Trypanosoma cruzi*: A review. *Mol. Biochem. Parasitol.* **240**, 111324 (2020).

45. Yamamoto, E., Kalli, A. C., Yasuoka, K. & Sansom, M. S. P. Interactions of pleckstrin homology domains with membranes: Adding back the bilayer via high-throughput molecular dynamics. *Structure* **24**, 1421–1431 (2016).
46. Le Huray, K. I. P., Wang, H., Sobott, F. & Kalli, A. C. Systematic simulation of the interactions of pleckstrin homology domains with membranes. *Sci. Adv.* **8**, 1–15 (2022).
47. Schoijet, A. C. *et al.* A *Trypanosoma cruzi* phosphatidylinositol 3-kinase (TcVps34) is involved in osmoregulation and receptor-mediated endocytosis. *J. Biol. Chem.* **283**, 31541–31550 (2008).
48. Gimenez, A. M. *et al.* Phosphatidylinositol kinase activities in *Trypanosoma cruzi* epimastigotes. *Mol. Biochem. Parasitol.* **203**, 14–24 (2015).
49. Bahia, D. *et al.* The TryPIKINome of five human pathogenic trypanosomatids: *Trypanosoma brucei*, *Trypanosoma cruzi*, *Leishmania major*, *Leishmania braziliensis* and *Leishmania infantum*—New tools for designing specific inhibitors. *Biochem. Biophys. Res. Commun.* **390**, 963–970 (2009).
50. Tirado-Duarte, D. *et al.* The Akt-like kinase of *Leishmania panamensis*: As a new molecular target for drug discovery. *Acta Trop.* **177**, 171–178 (2018).
51. Queiroz, R. M. L. *et al.* Quantitative proteomic and phosphoproteomic analysis of *Trypanosoma cruzi* amastigogenesis. *Mol. Cell. Proteom.* **13**, 3457–3472 (2014).
52. Becker, W., Bhattacharya, K. C., Gubensäk, N. & Zangger, K. Investigating protein-ligand interactions by solution nuclear magnetic resonance spectroscopy. *ChemPhysChem* **19**, 895–906 (2018).
53. Williamson, M. P. Using chemical shift perturbation to characterise ligand binding. *Prog. Nucl. Magn. Reson. Spectrosc.* **73**, 1–16 (2013).
54. Miao, R. *et al.* Akt: A potential drug target for metabolic syndrome. *Front. Physiol.* **13**, 822333 (2022).
55. Addie, M. *et al.* Discovery of 4-amino-N-[(1S)-1-(4-chlorophenyl)-3-hydroxypropyl]-1-(7H-pyrrolo[2,3-d]pyrimidin-4-yl) piperidine-4-carboxamide (AZD5363), an orally bioavailable, potent inhibitor of Akt kinases. *J. Med. Chem.* **56**, 2059–2073 (2013).
56. Roskoski, R. Properties of FDA-approved small molecule protein kinase inhibitors: A 2024 update. *Pharmacol. Res.* **200**, 107059 (2024).
57. Shen, Y. *et al.* Consistent blind protein structure generation from NMR chemical shift data. *Proc. Natl. Acad. Sci. U. S. A.* **105**, 4685–4690 (2008).
58. Shen, Y., Vernon, R., Baker, D. & Bax, A. De novo protein structure generation from incomplete chemical shift assignments. *J. Biomol. NMR* **43**, 63–78 (2009).
59. Lemmon, M. A. & Ferguson, K. M. Pleckstrin homology domains. *Curr. Top. Microbiol. Immunol.* **228**, 39–74 (1997).
60. Pettersen, E. F. *et al.* UCSF ChimeraX: Structure visualization for researchers, educators, and developers. *Protein Sci.* **30**, 70–82 (2021).
61. Maier, J. A. *et al.* ff14SB: Improving the Accuracy of protein side chain and backbone parameters from ff99SB. *J. Chem. Theory Comput.* **11**, 3696–3713 (2015).
62. Case, D. A. *et al.* AMBER 2020 (2020).
63. Fusani, L., Palmer, D. S., Somers, D. O. & Wall, I. D. Exploring ligand stability in protein crystal structures using binding pose metadynamics. *J. Chem. Inf. Model.* **60**, 1528–1539 (2020).
64. Jean, S. & Kiger, A. A. Classes of phosphoinositide 3-kinases at a glance. *J. Cell Sci.* **127**, 923–928 (2014).
65. Frech, M. *et al.* High affinity binding of inositol phosphates and phosphoinositides to the pleckstrin homology domain of RAC1 protein kinase B and their influence on kinase activity. *J. Biol. Chem.* **272**, 8474–8481 (1997).
66. Franke, T. F., Kaplan, D. R., Cantley, L. C. & Toker, A. Direct regulation of the Akt proto-oncogene product by phosphatidylinositol-3,4-bisphosphate. *Science* **275**, 665–668 (1997).
67. Wang, D. D., Ou-Yang, L., Xie, H., Zhu, M. & Yan, H. Predicting the impacts of mutations on protein-ligand binding affinity based on molecular dynamics simulations and machine learning methods. *Comput. Struct. Biotechnol. J.* **18**, 439–454 (2020).
68. Khazanov, N. A. & Carlson, H. A. Exploring the composition of protein-ligand binding sites on a large scale. *PLoS Comput. Biol.* **9**, e1003321 (2013).
69. Jumper, J. *et al.* Highly accurate protein structure prediction with AlphaFold. *Nature* **596**, 583–589 (2021).
70. Biondi, R. M. *et al.* High resolution crystal structure of the human PDK1 catalytic domain defines the regulatory phosphopeptide docking site. *EMBO J.* **21**, 4219–4228 (2002).
71. Pascucci, V., Labriola, C., Téllez-Inón, M. T. & Parodi, A. J. Molecular and biochemical characterization of a protein kinase B from *Trypanosoma cruzi*. *Mol. Biochem. Parasitol.* **102**, 21–33 (1999).
72. Krishna, R. *et al.* Generalized biomolecular modeling and design with RoseTTAFold All-Atom. *Science* **2528**, 1–17 (2024).
73. Yang, J. *et al.* Crystal structure of an activated Akt/protein kinase B ternary complex with GSK3-peptide and AMP-PNP. *Nat. Struct. Biol.* **9**, 940–944 (2002).
74. Yudushkin, I. Control of Akt activity and substrate phosphorylation in cells. *IUBMB Life* **72**, 1115–1125 (2020).
75. Akhooon, B. A., Gandhi, N. S. & Pandey, R. Computational insights into the active structure of SGK1 and its implication for ligand design. *Biochimie* **165**, 57–66 (2019).
76. Kornev, A. P., Taylor, S. S. & Ten Eyck, L. F. A helix scaffold for the assembly of active protein kinases. *Proc. Natl. Acad. Sci. U. S. A.* **105**, 14377–14382 (2008).
77. Meharena, H. S. *et al.* Deciphering the structural basis of eukaryotic protein kinase regulation. *PLoS Biol.* **11**, e1001680 (2013).
78. Stehle, J., Weisner, J., Eichhorn, L., Rauh, D. & Drescher, M. Insights into the conformational plasticity of the protein kinase Akt1 by multi-lateral dipolar spectroscopy. *Chem. A Eur. J.* <https://doi.org/10.1002/chem.202203959> (2023).
79. Salvador, R. R. S. *et al.* New carbonylhydrazide derivatives of 1H-pyrazolo[3,4-b]pyridine and trypanocidal activity. *An. Acad. Bras. Cienc.* **88**, 2341–2348 (2016).
80. Wu, Y. T. *et al.* mTOR complex 2 targets Akt for proteasomal degradation via phosphorylation at the hydrophobic motif. *J. Biol. Chem.* **286**, 14190–14198 (2011).
81. Thomas, C. C., Deak, M., Alessi, D. R. & Van Aalten, D. M. F. High-resolution structure of the pleckstrin homology domain of protein kinase B/Akt bound to phosphatidylinositol (3,4,5)-trisphosphate. *Curr. Biol.* **12**, 1256–1262 (2002).
82. James, S. R. *et al.* Specific binding of the Akt-1 protein kinase to phosphatidylinositol 3,4,5-trisphosphate without subsequent activation. *Biochem. J.* **315**, 709–713 (1996).
83. Milburn, C. C. *et al.* Binding of phosphatidylinositol 3,4,5-trisphosphate to the pleckstrin homology domain of protein kinase B induces a conformational change. *Biochem. J.* **375**, 531–538 (2003).
84. Craveur, P. *et al.* Protein flexibility in the light of structural alphabets. *Front. Mol. Biosci.* **2**, 1–20 (2015).
85. Hua, H. *et al.* Targeting Akt in cancer for precision therapy. *J. Hematol. Oncol.* **14**, 1–25 (2021).
86. Abeyrathna, P. & Su, Y. The critical role of Akt in cardiovascular function. *Vasc. Pharmacol.* **74**, 38–48 (2015).
87. Goyal, A., Agrawal, A., Verma, A. & Dubey, N. The PI3K-AKT pathway: A plausible therapeutic target in Parkinson's disease. *Exp. Mol. Pathol.* **129**, 104846 (2022).
88. Morel, M. *et al.* Compound library screening identified Akt/PKB kinase pathway inhibitors as potential key molecules for the development of new chemotherapeutics against schistosomiasis. *Int. J. Parasitol. Drugs Drug Resist.* **4**, 256–266 (2014).
89. Zimmerman Savill, K. M. *et al.* Distinct resistance mechanisms arise to allosteric vs. ATP-competitive AKT inhibitors. *Nat. Commun.* **13**, 1–17 (2022).

90. Oliveira, M. *et al.* FAIRLANE, a double-blind placebo-controlled randomized phase II trial of neoadjuvant ipatasertib plus paclitaxel for early triple-negative breast cancer. *Ann. Oncol.* **30**, 1289–1297 (2019).
91. Turner, N. C. *et al.* BEECH: A dose-finding run-in followed by a randomised phase II study assessing the efficacy of AKT inhibitor capivasertib (AZD5363) combined with paclitaxel in patients with estrogen receptor-positive advanced or metastatic breast cancer, and in a PIK3CA. *Ann. Oncol.* **30**, 774–780 (2019).
92. Landel, I., Quambusch, L., Depta, L. & Rauh, D. Spotlight on AKT: Current therapeutic challenges. *ACS Med. Chem. Lett.* **11**, 225–227 (2020).
93. Chiurillo, M. A., Jensen, B. C. & Docampo, R. Drug target validation of the protein kinase AEK1, essential for proliferation, host cell invasion, and intracellular replication of the human pathogen *Trypanosoma cruzi*. *Microbiol. Spectr.* <https://doi.org/10.1128/Spectrum.00738-21> (2021).
94. Bachmaier, S. & Boshart, M. Kinetoplastid AGC kinases. In *Protein Phosphorylation in Parasites: Novel Targets for Antiparasitic Intervention* (eds Doerig, C. *et al.*) 99–122 (Wiley-VCH Verlag GmbH & Co., 2014). <https://doi.org/10.1002/9783527675401.ch05>.
95. Page, N. *et al.* Identification and development of a subtype-selective allosteric AKT inhibitor suitable for clinical development. *Sci. Rep.* **12**, 15715 (2022).
96. Uhlenbrock, N. *et al.* Structural and chemical insights into the covalent-allosteric inhibition of the protein kinase Akt. *Chem. Sci.* **10**, 3573–3585 (2019).
97. Quambusch, L. *et al.* Covalent-allosteric inhibitors to achieve Akt isoform-selectivity. *Angew. Chem.* **131**, 18999–19005 (2019).
98. Weisner, J. *et al.* Kovalent-allosterische kinase-inhibitoren. *Angew. Chem.* **127**, 10452–10456 (2015).
99. Marion, D. *et al.* Overcoming the overlap problem in the assignment of 1H NMR spectra of larger proteins by use of three-dimensional heteronuclear 1H–15N Hartmann-Hahn-multiple quantum coherence and nuclear Overhauser-multiple quantum coherence spectroscopy: Application to interleukin 1. beta. *Biochemistry* **28**, 6150–6156 (1989).
100. Zuiderweg, E. R. P. & Fesik, S. W. Heteronuclear three-dimensional NMR spectroscopy of the inflammatory protein C5a. *Biochemistry* **28**, 2387–2391 (1989).
101. Vuister, G. W. & Bax, A. Resolution enhancement and spectral editing of uniformly 13C-enriched proteins by homonuclear broadband 13C decoupling. *J. Magn. Reson.* **435**, 69 (1991).
102. Olejniczak, E. T., Xu, R. X. & Fesik, S. W. A 4D HCCH-TOCSY experiment for assigning the side chain 1H and 13C resonances of proteins. *J. Biomol. NMR* **2**, 655–659 (1992).
103. Bax, A., Clore, G. M. & Gronenborn, A. M. 1H1H correlation via isotropic mixing of 13C magnetization, a new three-dimensional approach for assigning 1H and 13C spectra of 13C-enriched proteins. *J. Magn. Reson.* **88**, 425–431 (1990).
104. Kay, L. E., Xu, G.-Y., Singer, A. U., Muhandiram, D. R. & Forman-Kay, J. D. A gradient-enhanced HCCH-TOCSY experiment for recording side-chain 1H and 13C correlations in H2O samples of proteins. *J. Magn. Reson. Ser. B* **101**, 333–337 (1993).
105. Delaglio, F. *et al.* NMRPipe: A multidimensional spectral processing system based on UNIX pipes. *J. Biomol. NMR* **6**, 277–293 (1995).
106. Skinner, S. P. *et al.* CcpNmr AnalysisAssign: A flexible platform for integrated NMR analysis. *J. Biomol. NMR* **66**, 111–124 (2016).
107. Davis, A. L., Keeler, J., Laue, E. D. & Moskau, D. Experiments for recording pure-absorption heteronuclear correlation spectra using pulsed field gradients. *J. Magn. Reson.* **98**, 207–216 (1992).
108. Grzesiek, S. & Bax, A. Improved 3D triple-resonance NMR techniques applied to a 31 kDa protein. *J. Magn. Reson.* **96**, 432–440 (1992).
109. Kay, L. E., Xu, G. Y. & Yamazaki, T. Enhanced-sensitivity triple-resonance spectroscopy with minimal H2O saturation. *J. Magn. Reson. Ser. A* **109**, 129–133. <https://doi.org/10.1006/jmra.1994.1145> (1994).
110. Clubb, R. T., Thanabal, V. & Wagner, G. A constant-time three-dimensional triple-resonance pulse scheme to correlate intra-residue 1HN, 15N, and 13C' chemical shifts in 15N–13C-labeled proteins. *J. Magn. Reson.* <https://doi.org/10.1093/oseo/instance.00076703> (2017).
111. Schleucher, J., Sattler, M. & Griesinger, C. Coherence selection by gradients without signal attenuation: Application to the three-dimensional HNCO experiment. *Angew. Chem.* **32**, 1489–1491 (1993).
112. Wittekind, M. & Mueller, L. HNCACB, a high-sensitivity 3D NMR experiment to correlate amide-proton and nitrogen resonances with the alpha- and beta-carbon resonances in proteins. *J. Magn. Reson. Ser. B* **101**, 201–205. <https://doi.org/10.1006/jmrb.1993.1033> (1993).
113. Muhandiram, D. R. & Kay, L. E. Gradient-enhanced triple-resonance three-dimensional NMR experiments with improved sensitivity. *J. Magn. Reson. Ser. B* **103**, 203–216. <https://doi.org/10.1006/jmrb.1994.1032> (1994).
114. Grzesiek, S. & Bax, A. Correlating backbone amide and side chain resonances in larger proteins by multiple relayed triple resonance NMR. *J. Am. Chem. Soc.* **114**, 6291–6293 (1992).
115. Löhr, F. & Rüterjans, H. Correlation of backbone amide and side-chain 13C resonances in perdeuterated proteins. *J. Magn. Reson.* **156**, 10–18 (2002).
116. Montelione, G. T., Lyons, B. A., Emerson, S. D. & Tashiro, M. An efficient triple resonance experiment using carbon-13 isotropic mixing for determining sequence-specific resonance assignments of isotopically-enriched proteins. *J. Am. Chem. Soc.* **114**, 10974–10975 (1992).
117. Marion, D., Kay, L. E., Sparks, S. W., Torchia, D. A. & Bax, A. Three-dimensional heteronuclear NMR of 15N-labeled proteins. *J. Am. Chem. Soc.* **111**, 1515–1517 (1989).
118. Güntert, P., Mumenthaler, C. & Wüthrich, K. Torsion angle dynamics for NMR structure calculation with the new program DYANA. *J. Mol. Biol.* **273**, 283–298 (1997).
119. Herrmann, T., Güntert, P. & Wüthrich, K. Protein NMR structure determination with automated NOE assignment using the new software CANDID and the torsion angle dynamics algorithm DYANA. *J. Mol. Biol.* **319**, 209–227 (2002).
120. Schumann, F. H. *et al.* Combined chemical shift changes and amino acid specific chemical shift mapping of protein-protein interactions. *J. Biomol. NMR* **39**, 275–289 (2007).
121. Schrödinger. Maestro (2021).
122. Sastry, G. M., Adzhigirey, M. & Sherman, W. Protein and ligand preparation: Parameters, protocols, and influence on virtual screening enrichments. *J. Comput. Aided Mol. Des.* <https://doi.org/10.1007/s10822-013-9644-8> (2013).
123. Bowers, K. J. *et al.* Molecular dynamics: Scalable algorithms for molecular dynamics simulations on commodity clusters. In *Proceedings of the 2006 ACM/IEEE Conference on Supercomputing—SC '06* (ACM Press, 2006). <https://doi.org/10.1145/1188455.1188544>.
124. Lu, C. *et al.* OPLS4: Improving force field accuracy on challenging regimes of chemical space. *J. Chem. Theory Comput.* <https://doi.org/10.1021/acs.jctc.1c00302> (2021).
125. Hoover, W. G. Canonical dynamics: Equilibrium phase-space distributions. *Phys. Rev. A* **31**, 1695–1697 (1985).
126. Nosé, S. Molecular physics: An international journal at the interface between chemistry and physics a molecular dynamics method for simulations in the canonical ensemble. *Mol. Phys.* **52**, 255–268 (1984).
127. Martyna, G. J. *et al.* Constant pressure molecular dynamics algorithms. *J. Chem. Phys.* **101**, 4177–4189 (1994).
128. Darden, T., York, D. & Pedersen, L. Particle mesh Ewald: An N.log(N) method for Ewald sums in large systems. *J. Chem. Phys.* **100**, 1–5 (2020).

129. Hornak, V. *et al.* Comparison of multiple Amber force fields and development of improved protein backbone parameters. *PROTEINS Struct. Funct. Bioinform.* **65**, 712–725 (2006).
130. He, X., Man, V. H., Yang, W., Lee, T. S. & Wang, J. A fast and high-quality charge model for the next generation general AMBER force field. *J. Chem. Phys.* **153**, 6–12 (2020).
131. Evans, R. *et al.* Protein complex prediction with RNSC. *DeepMind* [https://doi.org/10.1007/978-1-61779-361-5\\_16](https://doi.org/10.1007/978-1-61779-361-5_16) (2021).
132. Friesner, R. A. *et al.* Glide: A new approach for rapid, accurate docking and scoring. 1. Method and assessment of docking accuracy. *J. Med. Chem.* **47**, 1739–1749 (2004).

## Acknowledgements

K.Z., T.P.K. and N.G. acknowledge the support of the field of excellence BioHealth at the University of Graz. L.O.J. acknowledges the support of CODI-Universidad de Antioquia, Coimbra Group Scholarship (University of Graz), as well as the Emerging Leaders in the Americas Program Canada (McGill University). We thank Yang Shen (NIDDK) for CS-Rosetta technical support. We thank Roberto Tejero (University of Valencia) for support with PSVS analysis. We thank Kyle Le Huray (University of Leeds) for providing the coordinate file of membrane-bound PH domain of *HsAkt1*, which we used for our illustrations. We also thank Lucy Maremmano for insightful discussions and motivation.

## Author contributions

\*K.S. and L.O.J. contributed equally to this work. A.S.S. performed and analyzed the MD simulations and docking studies; C.B. performed the AF and RoseTTaFold calculations; T.B.O., A.G. and L.O.J. performed and analyzed the DSF experiments; K.S., L.O.J. and N.G. performed the NMR experiments; K.S. and N.G. analyzed the NMR experiments and determined the structure (PDB: 8OZZ); L.O.J. performed the activity assays; K.S. and N.G. analyzed the NMR and AF structure; K.G., T.P.K., A.G., S.P., M.M., K.Z. and N.G. supervised the work; K.S., L.O.J. and N.G. conceptualized and wrote the manuscript. All authors contributed to the manuscript.

## Funding

The authors acknowledge the financial support by the University of Graz. This research was funded by the Austrian Science Fund (FWF) [<https://doi.org/10.55776/T1239> to N.G.; <https://doi.org/10.55776/DOC50> to K.Z.]. For the purpose of open access, the author has applied a CC BY public copyright licence to any Author Accepted Manuscript version arising from this submission. This research received funding from the Land Steiermark and the City of Graz (to K.Z.), the MINCIENCIAS-Colombia (Grant Number 111577757016, to M.M. and L.O.J.), and a Project Grant from the Canadian Institutes of Health Research (Grant Number PJT-155941, to A.G.). The authors also acknowledge the financial support by the University of Graz, the interuniversity programs NAWI Graz and BioTechMed for financial support. Financial contributions by the Land Steiermark infrastructure grant “Frontier NMR” (Project Number 1109) are also gratefully acknowledged.

## Competing interests

The authors declare no competing interests.

## Additional information

**Supplementary Information** The online version contains supplementary material available at <https://doi.org/10.1038/s41598-024-59654-8>.

**Correspondence** and requests for materials should be addressed to K.Z. or N.G.

**Reprints and permissions information** is available at [www.nature.com/reprints](http://www.nature.com/reprints).

**Publisher's note** Springer Nature remains neutral with regard to jurisdictional claims in published maps and institutional affiliations.



**Open Access** This article is licensed under a Creative Commons Attribution 4.0 International License, which permits use, sharing, adaptation, distribution and reproduction in any medium or format, as long as you give appropriate credit to the original author(s) and the source, provide a link to the Creative Commons licence, and indicate if changes were made. The images or other third party material in this article are included in the article's Creative Commons licence, unless indicated otherwise in a credit line to the material. If material is not included in the article's Creative Commons licence and your intended use is not permitted by statutory regulation or exceeds the permitted use, you will need to obtain permission directly from the copyright holder. To view a copy of this licence, visit <http://creativecommons.org/licenses/by/4.0/>.

© The Author(s) 2024